Experimental analysis of the flow characteristics of a pressure-atomised spray

Francisco Felis, Séverine Tomas, Ariane Vallet, Muriel Amielh, Fabien Anselmet

Experimental analysis of the flow characteristics of a pressure-atomised spray

F. Felis[a,b,c,1], S. Tomas[a], A. Vallet[b], M. Amielh[c], F. Anselmet[c]

[a] *Irstea, U.M.R. G-Eau, 361 rue J. F. Breton, B. P. 5095, 34196 Montpellier Cedex 5, France*

[b] *Irstea, U.M.R. ITAP, 361 rue J. F. Breton, 34196 Montpellier Cedex 5, France*

[c] *Aix Marseille Université, CNRS, Centrale Marseille, IRPHE U.M.R. 7342, 13384 Marseille Cedex 13, France*

Abstract

An experimental setup has been created to allow measurements of the properties of the gas phase, the liquid phase and the mixture in a pressure-atomised spray of water, in terms of both mean quantities and Reynolds stresses. This setup involves laser Doppler velocimetry for determining the velocity of either the gas or liquid phase, according to the parameters used, such as seeding or no-seeding of the ambient air, laser source power, photo-multiplier gains, ..., droplet tracking velocimetry for determining the velocity and characteristic size of the droplets, and a single optical probe for determining the mean volume fraction of the liquid, from which the liquid mean mass fraction and the mean density of the mixture are inferred. The experimental conditions, in particular in terms of liquid and gas Weber numbers, were chosen in a range for which the liquid phase turbulent kinetic energy should be mainly responsible for the liquid-jet primary break-up, these flow conditions lying within the second wind-induced atomization regime. Results reported herein are more specifically focused on the region ranging from 400 nozzle diameters to 800 nozzle diameters, where the liquid core is disrupted. They provide new information about the formation and properties of such pressure-atomised sprays, in particular in terms of the

[1] francisco.felis-carrasco@centrale-marseille.fr

role played by the Reynolds stresses resulting from the slip velocity between the liquid and the gas. The mean slip velocity is directly related to the turbulent flux of liquid. Such information will be used in the future to develop new turbulence models since very limited experimental information is so far available for these terms.

Keywords: Spray, Atomization, Experiments, Laser Doppler Velocimetry, Droplet Tracking Velocimetry, Optical Probe

---

1. Introduction

The atomization of a liquid jet, leading to the formation of a spray, occurs when a liquid-phase flow is injected into a gas-phase medium. This two-phase flow is considered non-miscible, meaning that the two phases do not form a mixture fluid and there are forces that keep a distinguishable interface between them. By the action of external forces on this interface, the liquid core breaks progressively into packets and droplets, causing its actual atomization into the gas phase. The forces present in this atomization process vary depending on the fluid properties and operating conditions (Dumouchel, 2008).

For the case considered herein, there is only one liquid phase and one gas phase present, no phase-change occurs and there are no compressibility effects. This case (see Section 3) corresponds to a typical system used in irrigation and/or pesticides aspersion consisting in a liquid-jet flow projected into ambient air. Upon this projection, the liquid flow splits into droplets which will ultimately reach the target soil or leaves.

The behaviour of the flow depends on several operational and environmental conditions, such as: geometry (in particular, nozzle diameter d_n and shape), flow rate, feeding pressure, turbulence, liquid rheology and wind velocity (but also temperature which will not be considered here), all of which have an impact on the droplets size, distribution and velocity. It is important then to understand the physical mechanisms by which the liquid atomization and droplets drifting occur to better conceive and/or improve the technological applications

in agriculture.

Compared to other domains, like fuel-injectors for combustion or bubbly-flows in boilers, the atomization problem in agricultural sprayers presents some specific features. For instance, the range of scales can go from the smallest scales of turbulence ($\sim 10^{-6}\,m$), passing through injector nozzle sizes of $\sim 10^{-3}\,m$, then to several meters of average range ($\sim 10^{0}\,m$) and even up to kilometers ($\sim 10^{3}\,m$) in the case of small droplets drift into the atmosphere. Since it is extremely difficult to study the whole problem, simplifications, sub-models, empirical relations, data integration, etc., still have to be made to tackle the final problem.

Throughout many years, the research development in liquid atomization for sprayers in agriculture has been conducted from a phenomenological approach, based on a large set of experiments that lead to empirical relations for some specific application. For example, the review by Al Heidary et al. (2014) shows some of these experimental approaches while the study by Salcedo et al. (2017) focuses on numerical simulations in an attempt to give a description of the flow. However, this kind of research methodology in every possible case is very expensive, both in time and resources. As results were found to be rather similar to other comparable situations, the most recent studies (Belhadef et al., 2012; Stevenin et al., 2016; Felis-Carrasco, 2017) have attempted to analyse the generic properties and to make comparison with results from the literature obtained for similar flow regimes in terms of Weber and Reynolds numbers.

For instance, the detailed velocity field issued from the Droplet Tracking Velocimetry (DTV) data obtained by Stevenin et al. (2016) gives some insights on the turbulent multiphase flow encountered in the irrigation problem, and it is now possible to compare the Reynolds stresses from the DTV with the turbulent kinetic energy from a turbulent RANS (Reynolds Averaged Navier-Stokes) model for the liquid phase. One interesting result is the anisotropy factor between the principal Reynolds stresses. Indeed, compared to a turbulent mono-phase round-jet or a spray encountered in combustion applications, where the anisotropy factor takes a value close to $\bar{R}_{22}/\bar{R}_{11} \approx 0.6$, this case shows a

value of $\bar{R}_{22}/\bar{R}_{11} \approx 0.05$ in the liquid phase, in the dispersed zone of the jet $(x/d_n > 500)$; where $\bar{R}_{11}$ is the axial component of the Reynolds stresses and $\bar{R}_{22}$ the lateral (radial) one. Even though such a behaviour has already been observed in particle-laden flows or circulating fluidised beds both experimentally (e.g. Rogers and Eaton, 1990) and numerically (e.g. Simonin, 1991; Özel et al., 2013), the turbulence anisotropy is generally much weaker (see the discussion in Stevenin et al. (2016)).

Analysing in more detail the velocity properties, both in terms of mean values and turbulent quantities, for each of the phases and for the mixture, is the main objective of the present study. For that purpose, a specific setup was created (see Felis-Carrasco (2017) for more details) that allows to determine separately the gas phase properties and the liquid phase properties, and in particular in terms of classes of droplet sizes, together with the slip between the phases. The present paper reports results associated with the global behaviour of the flow. In order to highlight the specific properties of sprays, the mass conservation and momentum equations will be briefly recalled in Section 2. The experimental setup and measurement techniques will be presented in Sections 3 and 4 respectively, before the discussion of results (Section 5) and the conclusion.

2. Mass conservation and momentum equations

The main objective of the present study is to determine the main characteristics of the various quantities which govern the development of the jet flow subject to atomization. These quantities concern the liquid phase, the gas phase and the global mixture. In the context of two-phase flows, budget equations must be derived using the quantity α_m which indicates whether the phase of index m is present (or not) at any particular point $\vec{x}$ and any particular instant t. It is assumed that at any point and any instant one phase only can be present. Therefore, $\alpha_m(\vec{x},t) = 1$ if phase m is present and $\alpha_m(\vec{x},t) = 0$ if phase m is not present, with $\sum_m \alpha_m(\vec{x},t) = 1$. Using this consideration, the budget equations can be derived in a quite straightforward way (e.g. Simonin,

1991; Ishii, 1975; Borghi and Anselmet, 2013). For phase m, the continuity (or mass conservation) equation then writes:

$$\frac{\partial(\rho_m \alpha_m)}{\partial t} + \frac{\partial(\rho_m \alpha_m u_{j,m})}{\partial x_j} = 0, \tag{1}$$

where ρ_m and $u_{j,m}$ stand for the density and the j-velocity component of phase m (in a space where $j = 1, 2, 3$ are the Cartesian coordinates indicators), with the assumption that there is no mass exchange between the phases for the situation considered here.

The Navier-Stokes (or momentum) equation writes:

$$\frac{\partial}{\partial t}\left(\rho_m \alpha_m u_{i,m}\right) + \frac{\partial}{\partial x_j}(\rho_m \alpha_m u_{i,m} u_{j,m}) = \frac{\partial(\alpha_m \sigma_{ij,m})}{\partial x_j} + f_{s,i,m-m'} \sigma_m^s, \tag{2}$$

where $f_{s,i,m-m'}$ represents the friction force between phase m and phase m' which applies on the interface s of volumetric density σ_m^s, and $\sigma_{ij,m}$ stands for the Cauchy stress tensor associated with phase m. In our case, both phases are Newtonian fluids. Note that gravity forces are neglected since the jet flow is inertial and aligned with gravity.

We then consider the statistical averages of these equations, in the present situation of a steady mean flow, and using Favre averages (such that, for any variable h, the Favre-averaged quantity $\widetilde{h}$ is weighted by the density : $\widetilde{h} = \frac{\overline{\rho h}}{\bar{\rho}}$), for the liquid phase (index L) or the gas phase (index G) respectively, or for the mixture velocity vector u_i.

For the liquid phase, these equations then become:

$$\frac{\partial \bar{\rho} \widetilde{Y} \widetilde{u}_{j,L}}{\partial x_j} = 0, \tag{3}$$

where $\widetilde{Y}$ denotes the liquid mass fraction and $\bar{\rho}$ the mean density of the mixture, with $\bar{\rho} = \bar{Y}\rho_L + (1 - \bar{Y})\rho_G$ and $\bar{Y}$ the liquid volume fraction such that $\bar{\rho}\widetilde{Y} = \rho_L \bar{Y}$, and

$$\frac{\partial(\bar{\rho}\widetilde{Y}\widetilde{u}_{i,L}\widetilde{u}_{j,L})}{\partial x_j} = \frac{\partial(\bar{Y}\bar{\sigma}_{ij,L} - \overline{\rho_L \alpha_L u_{i,L}^{''} u_{j,L}^{''}})}{\partial x_j} + \overline{\sigma_{ij,L} n_{j,L}} \bar{\sigma}^s, \tag{4}$$

where $u''_{i,L}$ denotes the velocity fluctuations in the context of Favre averaging, so that $\overline{u''}_{i,L} \neq 0$. The last term, $\overline{\sigma_{ij,L} n_{j,L}} \bar{\sigma}^s$, represents the mean contact force on the interface, which may be due to both pressure and viscous friction effects on the interface.

For the gas phase, they write :

$$\frac{\partial \bar{\rho}(1-\widetilde{Y})\widetilde{u}_{j,G}}{\partial x_j} = 0, \tag{5}$$

and

$$\frac{\partial(\bar{\rho}(1-\widetilde{Y})\widetilde{u}_{i,G}\widetilde{u}_{j,G})}{\partial x_j} = \frac{\partial((1-\bar{Y})\bar{\sigma}_{ij,G} - \overline{\rho_G \alpha_G u''_{i,G} u''_{j,G}})}{\partial x_j} + \overline{\sigma_{ij,G} n_{j,G}} \bar{\sigma}^s. \tag{6}$$

And, for the mixture, where the Favre-averaged mixture velocity field $\widetilde{u}_i$ is given by

$$\widetilde{u}_i = \widetilde{Y}\overline{u}_{i,L} + (1-\widetilde{Y})\overline{u}_{i,G}, \tag{7}$$

the equations write :

$$\frac{\partial \bar{\rho}\widetilde{u}_i}{\partial x_i} = 0 \tag{8}$$

and

$$\frac{\partial \bar{\rho}\widetilde{u}_i\widetilde{u}_j}{\partial x_j} = -\frac{\partial \bar{p}}{\partial x_i} + \frac{\partial \widetilde{\tau}_{ij}}{\partial x_j} - \frac{\partial \bar{\rho}\widetilde{u''_i u''_j}}{\partial x_j}, \tag{9}$$

where the capillarity forces have been neglected and the Favre averaged viscous stress tensor is given by $\widetilde{\tau}_{ij} = \bar{\mu}(\frac{\partial \widetilde{u}_i}{\partial x_j} + \frac{\partial \widetilde{u}_j}{\partial x_i} - \frac{2}{3}\frac{\partial \widetilde{u}_k}{\partial x_k}\delta_{ij})$, with the dynamic viscosity $\bar{\mu} = \bar{Y}\mu_L + (1-\bar{Y})\mu_G$. For the mixture, if viscous and pressure effects can be neglected when the jet flow has reached a self-similar behaviour for a large Reynolds number, we then obtain budget equations which are formally similar to those for a single phase flow. However, the Reynolds stress $\widetilde{R}_{ij} = \widetilde{u''_i u''_j}$

involves contributions from the liquid and gas phases, and it can be written as (see Appendix A for each particular definition):

$$\widetilde{R}_{ij} = \widetilde{Y}\bar{R}_{ij,L} + (1-\widetilde{Y})\bar{R}_{ij,G} + \widetilde{Y}(1-\widetilde{Y})\bar{R}_{ij,S}, \tag{10}$$

where:

- $\overline{u'_{i,L}u'_{j,L}}$: Liquid Reynolds stresses (or $\bar{R}_{ij,L}$);
- $\overline{u'_{i,G}u'_{j,G}}$: Gas Reynolds stresses (or $\bar{R}_{ij,G}$);
- $\bar{u}_{i,S}\bar{u}_{j,S}$: Slip Reynolds stresses (or $\bar{R}_{ij,S}$).

Note that in Reynolds averaged quantities, fluctuations $u'_{i,L}$ or $u'_{i,G}$ are then involved. The slip Reynolds stresses $\bar{R}_{ij,S}$ are defined simply as the products of the slip-velocities, $\bar{u}_{i,S}\bar{u}_{j,S}$, where each component is:

$$\overline{u}_{i,S} = \overline{u}_{i,L} - \overline{u}_{i,G} = \frac{\widetilde{u''_i Y''}}{\widetilde{Y}(1-\widetilde{Y})}. \tag{11}$$

In the present study, a direct measure of the fluctuations Y'' could not be obtained. The turbulent mass fluxes $\widetilde{u''_i Y''}$ are then calculated indirectly using Eq. 11, using $\overline{u}_{i,G}$ and $\overline{u}_{i,L}$, the gas and liquid mean velocity fields respectively, together with the liquid mass fraction $\widetilde{Y}$. A detailed discussion related to experimental values of these turbulent fluxes and their modelling in the RANS context can be found in Felis-Carrasco (2017).

3. Study case

A circular nozzle of diameter $d_n = 1.2\,mm$ is used as a simplified injector. To avoid any extra difficulty on the estimation of the boundary layer inside the nozzle, a borosilicate glass is chosen for the material so the roughness of the interior walls is considered negligible. In the same way as Wu et al. (1992), Sallam et al. (2002) and others mentioned in the review on round jets by Dumouchel (2008), the nozzle length L_n is also chosen in order to obtain a fully developed turbulent pipe flow, here $L_n/d_n = 50$.

ρ_L	Water density	998.3	kg/m^3
ρ_G	Air density	1.205	kg/m^3
ν_L	Water kinematic viscosity	1.004×10^{-6}	m^2/s
ν_G	Air kinematic viscosity	15.11×10^{-6}	m^2/s
σ	Water-Air surface tension	0.073	N/m

Table 1: Physical properties of the study case in SI-units at normal conditions.

Liquid water is injected into still air (see Tab. 1 for the physical properties taken at 297 K, 1 atm), where the injection velocity is aligned with gravity, pointing downwards. An injection mean bulk velocity of $\bar{u}_J = 35\, m/s$ (subscript J means at the nozzle exit) is fixed at the maximum possible value that insures there is no cavitation inside the injector.

Having these basic physical properties and operating conditions, three main dimensionless quantities can be constructed as a function of the forces that intervene in the atomization process. First, the Reynolds number, defined at the nozzle exit as $Re = \frac{\bar{u}_J d_n}{\nu_L}$, allows to identify if the liquid flow inside the injector is turbulent. Secondly, the liquid-phase based Weber number, $We_L = \frac{\rho_L \bar{u}_J^2 d_n}{\sigma}$, and the gas-phase based one, $We_G = \frac{\rho_G \bar{u}_J^2 d_n}{\sigma}$, weight the importance of the surface tension once the flow is in contact with the surrounding air. And, finally, the Ohnesorge number, defined by $Oh = \frac{\rho_L \nu_L}{\sqrt{\rho_L \sigma d_n}} = \frac{\sqrt{We_L}}{Re}$, [R03-C02] can be used to determine the range of shapes the liquid packets or droplets can take in the atomization process. Choosing $Re = 41833$ and $L_n/d_n = 50$ makes the internal flow fully turbulent and ensures that the boundary layer inside the nozzle is fully developed upon any upstream conditions. And finally, as a consequence of choosing $We_L = 20158$, $We_G = 24.3$ and $Oh = 0.0034$, the liquid phase turbulent kinetic energy should be mainly responsible for the liquid-jet primary break-up (Sallam et al., 2002), being the later atomization inside the second wind-induced atomization regime (Dumouchel, 2008).

The complete breakup and atomization processes of this study case can be visualised in Fig. 1, where shadow images at the centerline of the liquid-jet are

obtained in the range of $x/d_n = 0 - 800$. The experimental technique used to obtain these images will be detailed later. From the start of the liquid jet, small ligaments can be seen at $x/d_n = 0$ close to the nozzle, as Wu and Faeth (1995) explain, they are related to the boundary layer inside the nozzle, where their sizes are found to be proportional to the turbulent eddies inside the injector. Downstream, at $x/d_n = 150$, some helical structures appear, Hoyt and Taylor (1977) explained these structures by the amplification of an helical instability mode, where aerodynamic effects start to play a more significant role in the turbulent breakup regime. Further more, at $x/d_n = 200$, a continuous liquid core is hard to find in the series of images, marking the end of the primary breakup, leaving large packets of liquid and secondary breakup events that happen downward. The dispersed part of the atomised liquid jet is observable for $x/d_n > 400$, where those large packets are broken into more spherical droplets up to $x/d_n = 800$.

Following the original works by Wu et al. (1992) and Sallam et al. (2002), an immediate analysis of the atomization regime is reported by looking at the breakup events from Fig. 1. [R01-C01] From $x/d_n < 100$, there are no visible core breakup events, whereas for $x/d_n > 400$ the liquid core appears always broken in the image series. Each of the images is taken from a series of 1000 at each point, from where the numbers of breakup events are counted at each position in the region from $x/d_n = 100$ to $x/d_n = 300$. The ratio of the number of events N_b to the total number of images N_T should follow the probability that the average breakup length $\bar{L}_c$ be less than or equal to the given position from the nozzle. The result of this calculation is presented in Fig. 2, where every set of images from $x/d_n = 100$ to $x/d_n = 300$ fits well a Normal distribution, with a mean value of $\bar{L}_c/d_n = 219$. As a reference, the relation given by Sallam et al. (2002), based on a best-fit of several experiments on the same regime, gives $\frac{\bar{L}_c}{d_n} = 8.51We_L^{0.31} = 203$.

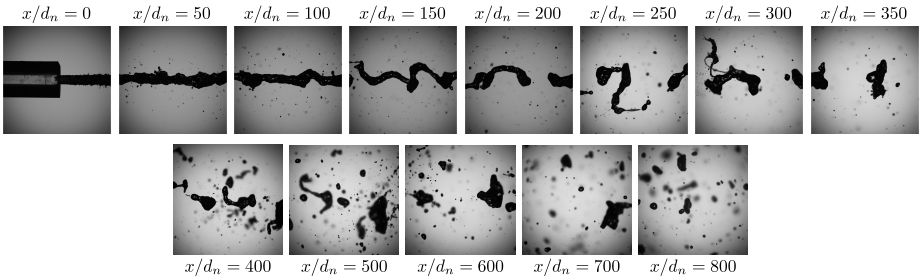

Figure 1: Shadow images on the jet centerline from $x/d_n = 0$ to $x/d_n = 800$ (non-synchronised images).

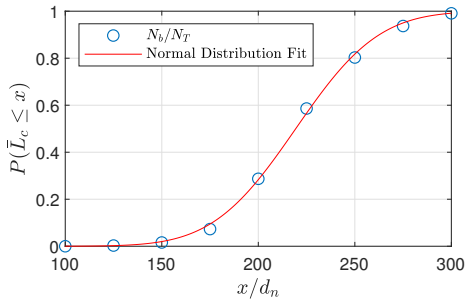

Figure 2: Empirical probability distribution for observed liquid-core breakup events observed in the range $x/d_n = 100 - 300$. Experimental points from a series of 1000 images in blue circles; Normal distribution fit in red line.

4. Experimental setup

The liquid jet is characterised using several optical experimental techniques. The aim is to obtain a complete description of the liquid jet described in the previous section, where an approximation to the velocity field is obtained from $x/d_n = 0$ to $x/d_n = 800$.

As presented in Section 2, a multiphase flow is fully described if the velocity field $u_{i,m}(\vec{x}, t)$ and the phase presence indicator $\alpha_m(\vec{x}, t)$ are known for each phase m. This goal is in general very difficult to achieve in practical applications, both experimentally and numerically, as the flow is most commonly turbulent and the multiphase nature of the flow makes the visual access to experimental instruments very challenging (Boutier, 2012).

It is important then to state from the beginning which part of $u_{i,m}$ and α_m is obtainable in this study. Moreover, given the turbulent nature of the liquid jet and the atomization regime detailed in the study case section, the description is reduced to space/time averaged field quantities, obtained from the experimental techniques used.

Three different techniques were used to measure the liquid and gas velocity fields, $u_{i,L}$ and $u_{i,G}$ respectively, and the mean liquid volume fraction $\overline{Y}$. The instruments related to these measurement techniques were mounted into the same experimental setup as shown in Fig. 3, along with the physical location of the measurement points for each campaign.

The optical probe (OP) provides the mean liquid mass fraction $\widetilde{Y}$ (or $\widetilde{\alpha}_L$) and the mean liquid volume fraction $\overline{Y}$ (or $\overline{\alpha}_L$). A special configuration of LDV (Laser Doppler Velocimetry) allows to obtain a distinction between $u_{i,L}$ and $u_{i,G}$, for both the mean and fluctuating components to some extent. Going deeper, a custom DTV (Droplet Tracking Velocimetry) algorithm can dissect $u_{i,L}$ by classes of droplet diameter (k), $u_{i,(k)}$. If a proper average over these fields is used, then a reconstruction of Eq. 7 and Eq. 10 can be made to fully characterise the gas-liquid jet mixture.

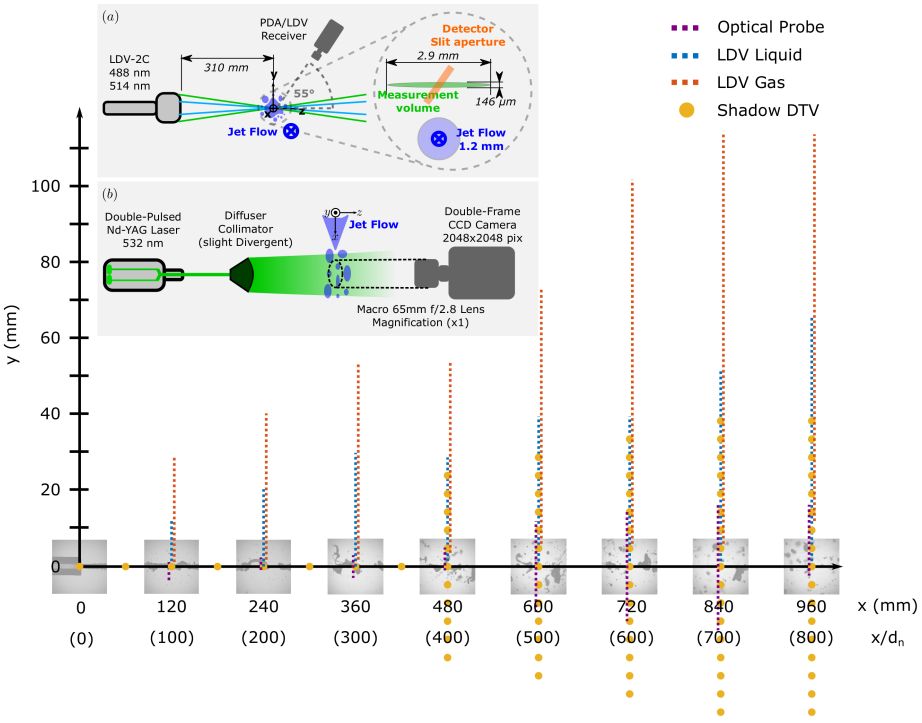

Figure 3: Complete extent of the measurement campaigns: Optical Probe, LDV on the liquid phase, LDV on the gas phase and DTV by shadow images. Schematic view of the experimental setup for: (a) Two-component LDV with the jet and measurement volume representation; (b) DTV using consecutive shadow images.

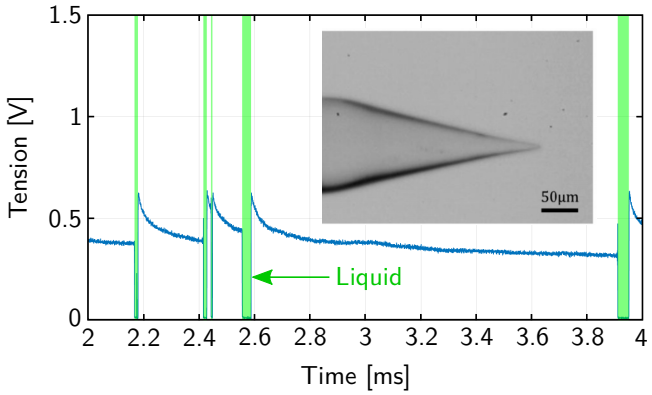

Figure 4: Typical signal delivered by the optical probe (jet centerline, $x/d_n = 600$, sampled at 3.9 MHz, $\overline{Y} \approx 0.03$). The blue line corresponds to the OP signal, and the green shaded zones to the signal portions corresponding to droplets.

4.1. Optical Probe (OP)

To reconstruct first the liquid volume fraction $\overline{Y}$, a measurement campaign using an optical probe was performed. The probe is a Monomode M2 (M-A02-3 & M-A03-4) from the M2-Spray-Analyser provided by A2 Photonic Sensors. The measurement principle of this mono-probe is by discriminating if the tip is submerged or not in liquid, with a known refractive index. A laser source is used to illuminate the tip via an optical fibre, and the photo-detector compares the amount of reflected light received with the non-wetted baseline. The size of the probe is shown in Fig. 4, this probe can detect droplets of sizes $d > 5\mu m$.

This void fraction $(1 - \overline{Y})$ is determined from the high level parts of the signal, corresponding to time instants for which the probe is within air pockets. Even though sophisticated signal analysis may provide the velocity and chord length of each droplet based on the methodology developed by Cartellier (1992), only the information related to the void fraction was retained (see Fig. 4), based on a threshold level criterion. [R01-C02][R01-C04][R03-C10] A sensitivity analysis was made with respect to the optimal threshold level to both detect small droplets and not overshoot the de-wetting process of bigger ones. The sampling frequency was then set to $3.9\,MHz$, allowing to accurately sample

both extreme cases. With this frequency and threshold level, the statistical uncertainty for the liquid volume fraction $\overline{Y}$ is less than 5%.

Finally, the liquid mass fraction was obtained using Eq. 12, where $\bar{\rho} = \bar{Y}\rho_L + (1-\bar{Y})\rho_G$:

$$\widetilde{Y} = \frac{\rho_L \overline{Y}}{\bar{\rho}}. \tag{12}$$

Because this measurement campaign was only meant to be exploratory at first, the measurement domain and number of physical points was roughly defined as shown in Fig. 3, where the traverse mechanisms only covered the dense part of the spray. For profiles at $x/d_n = 200$, $x/d_n = 300$, $x/d_n = 400$ and $x/d_n = 800$ the traverse mechanisms could not be used and a manual translation stage has been used (13 mm travel; 10 μm precision) . To fully exploit these results later, the values given by these measurement points were interpolated to the same grid defined by the LDV and DTV campaigns. [R01-C03] The results consist in complete lateral profiles across the liquid jet. For both techniques (LDV and DTV), the reliability accuracy is $\pm 0.02\,mm$ and the absolute position accuracy is $0.08\,mm$, with a total displacement range of $300\,mm$. Starting from $x/d_n = 100$ and up to $x/d_n = 800$, an exponential fit was applied of the form:

$$\widetilde{Y}(y) = A \cdot e^{-b \cdot y^c}, \tag{13}$$

where A, b and c are the fitting parameters and y the lateral (radial) position. Once the profiles are reconstructed in $\widetilde{Y}$, the same transformation was used to express $\overline{Y}$ (Eq. 12). This procedure is illustrated in Fig. 5, where examples of reconstruction of the lateral profiles at $x/d_n = 400$, $x/d_n = 600$ and $x/d_n = 800$ with remarkable likelihood are shown. Although the choice of the fit (Eq. 13) is not discussed further, the simplicity of the form allows to quickly infer the axial evolution and the half-width of the liquid jet, which are considered later on for the global analysis (Section 5.5).

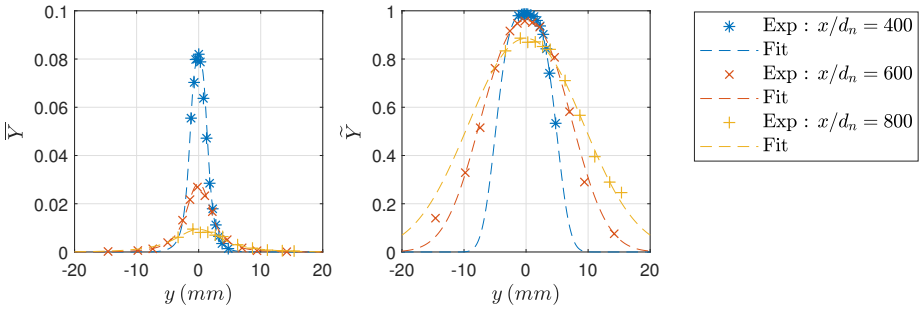

Figure 5: Liquid volume fraction $\overline{Y}$ and calculated liquid mass fraction $\widetilde{Y}$ obtained by the Optical Probe (OP) at $x/d_n = 400$, $x/d_n = 600$ and $x/d_n = 800$. Experimental points in markers; fit using Eq. 13 in the dashed lines.

4.2. Laser Doppler Velocimetry (LDV)

A two component Laser Doppler Velocimeter (LDV) from a 2D-PDA (Phase Doppler Anemometer) is used to determine the liquid phase (water) and gas phase (air) velocity fields. As Fig. 1 shows, the attempt to measure the liquid velocity field $u_{i,L}$ and the gas phase velocity field $u_{i,G}$ seems quite challenging for the study case described in Section 3. [R03-C12] [R03-C13] For example, to measure inside the liquid core from the nozzle injection point at $x/d_n = 0$ and up to $x/d_n = 400$, seeding particles should be present in the liquid phase, where the LDV measurement volume must penetrate the liquid to illuminate those particles, while the receiving optics must have a clear view of this region to capture accurately Doppler bursts from these tracers. In the dispersed region of the spray ($x/d_n = 400 - 800$), although the liquid core is no longer present, a PDA measurement technique would only validate small and almost spherical droplets, leaving a large portion of non-spherical ones out of the analysis. To measure the velocity field of the gas phase, seeding particles must be present in the gas around the liquid, where the burst spectrum analyser (BSA) must be capable of making a clear distinction between the signal from a water droplet and the desired refraction mode from a small tracer.

The LDV setup consists in a two component (LDV-2C) system from Dantec Dynamics with an Argon-ion Coherent 306S laser source. A Dantec-Dynamics

60×11 transducer separates and conducts the beams at $488\,nm$@$1.8W$ and $514.5\,nm$@$2.8W$. A $310\,mm$ focus-length optics is used for the emitter and a $400\,mm$ for the receiver, forming a LDV measurement volume of $0.146 \times 0.146 \times 2.9\,mm^3$ along the principal x, y, z directions respectively. The third direction dimension is then reduced again by configuring the LDV in forward scattering mode, similar to a PDA configuration at $\Phi = 55°$, where a $200\,\mu m$ pinhole in the receiver optics cuts the classic LDV ellipsoid measurement volume into almost a rhombohedron as shown in Fig. 3-(a). A Burst Spectrum Analyser (BSA) P60, also from Dantec Dynamics, is used to acquire the raw LDV data and analyse them.

Some key details on the specific configuration for measuring the liquid and gas phases is presented here. [R01-C05] A more detailed step-by-step configuration can be found in Felis-Carrasco (2017). As mentioned before, the goal is to capture the liquid phase velocity field $u_{i,L}$ and the gas phase velocity field $u_{i,G}$. When measuring only in the liquid phase, the LDV captures as a time series the velocity of the liquid/gas interface of large liquid packets or small droplets. Because no particles are seeded in the liquid phase, the forward scattering mode captures either the velocity of droplets, or ripples on the interface (for very large packets of liquid). To capture the gas phase, a second configuration uses olive-oil mist as tracers for the gas around the liquid, where the processing unit captures the velocity of small oil droplets of $\sim 1 - 2\,\mu m$ and the original liquid droplets. [R01-C06] To ensure their uniformity, these oil droplets are seeded all around the jet inside an atmosphere controlled room.

As described by Mychkovsky et al. (2012); Mychkovsky and Ceccio (2012) in a fluidised bed study, a distinction between the tracers and the real particles can be made by looking at the Doppler burst signal pedestal. If one type of particles is considerably bigger than the other, the burst is expected to have a bigger carrier pedestal too. In a transposition from their case, here, the background gas phase is seeded with very small tracers compared to the poly-dispersed liquid droplets, so the same distinction is expected to exist. Other authors have also worked with this technique on bubbly flow, like those mentioned in the review

Table 2: Global LDV BSA setup for liquid and gas phases analysis.

Configuration	**Laser Power**	**PM Gain**	**SNR**	**BP-Filter**	**Seeded air**
Liquid Low-S	0.6 W	600-800 V	4 dB	Span based	No
Liquid High-S	0.6 W	1000-1200 V	4 dB	Span based	No
Gas High-S	1.1 W	1200-1400 V	8 dB	Span based	Yes

performed by Joshi et al. (2017), where the main difficulty for this kind of LDV setup is to capture a proper Doppler signal from the tracers in the carrier phase, when a heavy dispersed second phase is present.

However, the available BSA-P60 from Dantec Dynamics does not allow to record the Doppler burst pedestal, as this signal is eliminated from the processor at the beginning of the burst analysis inside the BSA. With this in mind, a second strategy is developed by doing two sets of measurements: a first campaign without seeded particles in the gas phase, therefore measuring only in the liquid phase; and a second one with the seeded particles, but avoiding to get too close to the jet axis, where a large concentration of water droplets is present.

Three different configurations for the laser source power (LP), photo-multiplier high-voltage (PM), accepted signal-to-noise ratio (SNR) and band-pass filter (BP) for the Doppler frequency are selected and shown in Tab. 2. [R01-C05] The average sampling rate is highly variable both in the stream-wise and radial directions. Because of this, either a long acquisition time (low data-rate) of 5 minutes or a maximum number of 1000000 events (high data-rate) is demanded for each measurement point.

Given that the LDV processing module does not allow an actual separation of the signal acquired in the gas phase configuration (olive-oil particles), relevant assumptions should be considered when looking at the gas-phase velocity field. First, it is noticed that a much greater PM gain is needed to detect the olive-oil particles in the raw Burst-Doppler signal. By increasing this value, along with the desired signal to noise ratio limit (SNR), it yields a large data-rate only for

oil droplets, where, although large non-spherical objects have a higher intensity, they are seen much noisier and therefore they are more likely to be rejected by the SNR criterion. However, there will always be some water droplets that are counted as part of the gas signal. Secondly, because the signal intensity from the water droplets/packets is higher, the desired gain in the PM sensitivity for capturing the tiny gas tracers sets a [R03-C16] limit on the positioning of the measurement volume. Indeed, the measurement volume for the gas phase campaign must not be placed in regions with large liquid elements. So, no overlapping between gas and liquid profiles is achieved when a large concentration of water droplets is present, to avoid damage to the PMs. Fig. 6 shows this configuration graphically, where the LDV measurement domain across the radial (lateral) direction is superimposed over shadow images at $x/d_n = 600$. Indeed, at this longitudinal position, no LDV measurements can be made for $y < 6\,mm$, because the anode current passing through the PM is too high, probably from the light reflection or refraction coming from the large packets of liquid present in that region.

Another restriction imposed by the LDV configuration in forward scattering mode arises from the configuration shown in Fig. 3 and Fig. 6. The reflection/refraction mode from those large droplets interfere with the receiving LDV optics in the PDA configuration, therefore, only radial (lateral) profiles are acquired in this measurement campaign, starting from the spray centerline. On the contrary, the Optical Probe (OP) in Section 4.1 and Droplet Tracking Velocimetry (DTV) in Section 4.3 include complete lateral profiles. Nevertheless, complete 2D-LDV measurements were performed in a 2D grid at $x/d_n = 400$ to carefully align the LDV measurement axis components, checking that: $\bar{u}_{1,L}$ is symmetric, $\bar{u}_{2,L}$ anti-symmetric and $\bar{u}_{2,L} = 0$ at $y = 0$ and $\bar{R}_{12,L}$ is also anti-symmetric and $\bar{R}_{12,L} = 0$ at $y = 0$, ensuring the cylindrical axisymmetry of the spray. Corrections were then introduced iteratively using a pan/tilt micro-metric stage.

Finally, to account for the possible bias related to the irregular sampling of the LDV data, the weighted average procedure proposed by Buchhave et al.

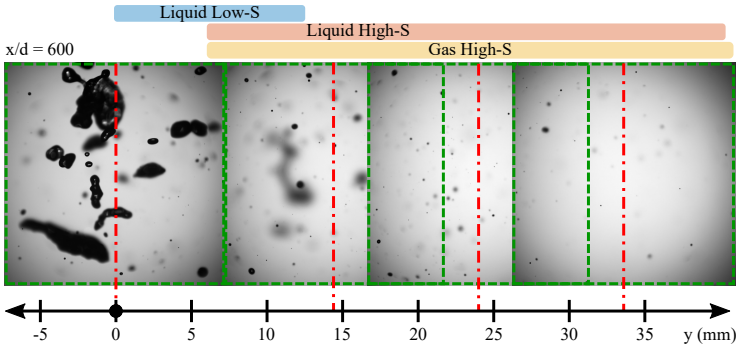

Figure 6: Superimposition of shadow images and the LDV measurement points. Green dashed frames represent each image border. Red dashed line, the image centerline.

(1979) was used in both liquid and gas series, [R01-C07] where the averaged quantities are weighted by the particle transit time *tt* inside the LDV measurement volume. However, the effect of this analysis was found to be negligible in the present case and is not shown in the results.

4.3. Droplet Tracking Velocimetry by Shadowgraphy (DTV)

Shadow images are used to run a custom Droplet Tracking Velocimetry (DTV) algorithm on the dispersed regions of the spray and to visualise the liquid column breakup closer to the nozzle. These images are generated by the shadow of the liquid, projected into a double-frame camera in the presence of a collimated background light, mounted as shown in Fig. 3. The system captures two consecutive images (frame 1 and frame 2) at a very short inter-frame time (time between pulses *tbp*). This process is repeated N_T times at a global acquisition frequency (f_a), forming a time series of images. In this approach, $f_a << \frac{1}{tbp}$, so two consecutive pairs of frames are not correlated in time, but a detection and matching of particles/features can be made in-between the two frames of a pair.

The background light for the shadow images is generated by a double-pulsed laser source, consisting of a Litron Nd-YAG of $135\,mJ$ ($532\,nm$). The light is then conducted via an optical fibre to a diffuser/collimator, generating a non-coherent uniform background (*ShadowStrobe* system from Dantec Dynamics).

An HiSense 4M-C CCD camera mounted with a Canon MP-E 65 mm f/2.8 lens is used, where the magnification is set to $\times 1$ with a working distance of $101\,mm$, making the imaging system effectively telecentric. The camera captures 12-bit depth grey-scale images at 2048×2048 pixels in a double-layer CCD sensor. With this optical arrangement, the scale resolution is $139\,pix/mm$ (or $7.194\,\mu m/pix$), transformed into a Field-of-View (FOV) of $14.73 \times 14.73\,mm^2$. The acquisition frequency for a pair of images is set to $f_a = 5\,Hz$, [R01-C09] with a total of $N_T = 1000$ pairs of frames acquired for every measured point. The time between pulses varies depending on the mean velocity of the objects inside the frame. This is an important parameter to set, because it should be large enough to let the droplets move in-between frames, but not too much so that no significant changes to the overall form and/or location pattern of the objects inside the frame are produced. Every pair of images is then analysed to measure each droplet's characteristic size, shape and position.

In a classical detection and segmentation technique, a global thresholding method is used to binarize the whole image at an optimal grey-level i (thresholding), resulting in many isolated blobs that can be identified as droplets (Otsu, 1979). The use of this method however is not well suited for shadow images of a dense or poly-dispersed spray, where a mixture of droplets with different sizes and defocusing projections are superposed to form the image. By looking at the previously presented images in Fig. 1, if the global threshold is set too high (towards the whites), many droplets can be detected at once, but they will probably be detected as a cluster, distorting their size estimation; on the contrary, if the threshold is too low (towards the blacks), only sharp in-focus droplets can be detected, leaving many others out of the analysis.

To overcome this detection issue, a custom DTV algorithm was constructed based on the procedure developed by Yon (2003), including the later size correction and depth-of-field (DOF) calibration developed by Fdida and Blaisot (2010). Instead of relying on the global thresholding technique to segment the images, a local analysis is performed instead, ensuring that in-focus and out-of-focus droplets are detected. Later, a size correction function is introduced,

together with the DOF calibration, ensuring that the population of droplets detected are in the same measurement volume. The overall procedure is shown in Fig. 7 and it is detailed step-by-step in the following sub-sections.

4.3.1. Segmentation

Fig. 7-a shows a composition, where both frames are superimposed (only for reference): in magenta colour (frame 1) and green colour (frame 2). For this case, a short $tbp = 5\,\mu s$ was used, so high velocity droplets do not move/deform much in between frames. A portion of frame 1 is shown in Fig. 7-b as an example, this image is referred to as the original image (Im_{org}) in the present analysis.

A Mexican-hat kernel function was applied as a filter to the original image (Im_{org}), the goal is to amplify the image gradient at the borders, increasing the contrast of the out-of-focus objects (Im_{wt}). This first procedure allows to identify every object for a local analysis, as the background of Fig. 7-c shows. Following the analysis detailed by Yon (2003), every object is isolated and analysed locally. A local image is created for every object, by applying the binary mask of Fig. 7-c to Im_{org}, resulting in a subset of smaller images Im_{ROI} (Region of Interest of local images).

4.3.2. Local analysis

The local region of interest (Im_{ROI}) is transformed using a linear transfer function, moving from a 12-bit grey-level space with integer-type values in the range $[0-4095]$, into the local image to analyse (Im_{loc}), with double-type values in the range $[0-1]$. In this subspace, the grey-levels are defined as i, where i_{min} and i_{max} are the minimum (dark) and maximum (bright) values from the previous 12-bit space.

From now, these local images are the only candidates to become accepted droplets. To continue the analysis, the contrast ratio defined as $C = (i_{max} - i_{min})/(i_{max} + i_{min})$ in Im_{loc} is calculated. Then, if $C < 0.1$, the droplet is considered too blurry and it is rejected from the analysis. Passing this first test,

Im_{loc} is now normalised, meaning that the measured global grey levels are still in the range $0 < i < 1$, but the limits are stretched to $i_{min} = 0$ and $i_{max} = 1$, with no saturation.

Yon (2003), and later Fdida and Blaisot (2010), developed a method to define and measure a characteristic size d_m for out-of-focus droplets by shadow images. This method is based on the binarisation of the previous normalised Im_{loc} image at different grey-levels i. As Fig. 7-d shows, these levels correspond to several iso-contours (w) of intensity (i) in the image, where the following ones are extracted: $w_{i=0.25}$, $w_{i=0.50}$, $w_{i=0.61}$ and $w_{i=0.77}$. [R01-C10] These contours are used to both represent the linear part of the grey-level gradient between $w_{i=0.25}$ and $w_{i=0.77}$ (see Fig. 7-e), and the limit at $w_{i=0.61}$, which allows an injective calibration function (contrary to the standard $w_{i=0.50}$) in the same way as Fdida and Blaisot (2010). The size correction and depth-of-field calibration are described later in Section 4.3.4.

4.3.3. Matching algorithm

Using the 3D representation described by Daves et al. (1993), the equivalent diameter $d_{[30]}$ is calculated. The method infers a volume equivalent diameter using $d_{[30]} = \sqrt[3]{\frac{6V_{0.61}}{\pi}}$, where $V_{0.61}$ is the reconstructed volume from the extracted $w_{i=0.61}$ contour. Other quantities are also kept for further analysis, like the principal axes, orientation and eccentricity of the objects.

Using the centroids from every droplet detected, on (x, y) coordinates in the pair of images, the point matching algorithm from Gold et al. (1998) was used to estimate their velocity. [R01-C11] Although the centroids located in each pair of frames are close-by, a simple nearest-neighbour matching yields too many wrong pairs when many small particles are clustered together. To improve this, the implemented method minimises a target cost function by applying 2D shear, rotation and translation to the cloud of points detected from Frame 1 into Frame 2, yielding a nearly perfect match in almost every tested scenario. Finally, knowing the scale resolution and the time between images, the velocity vector of every droplet can be estimated.

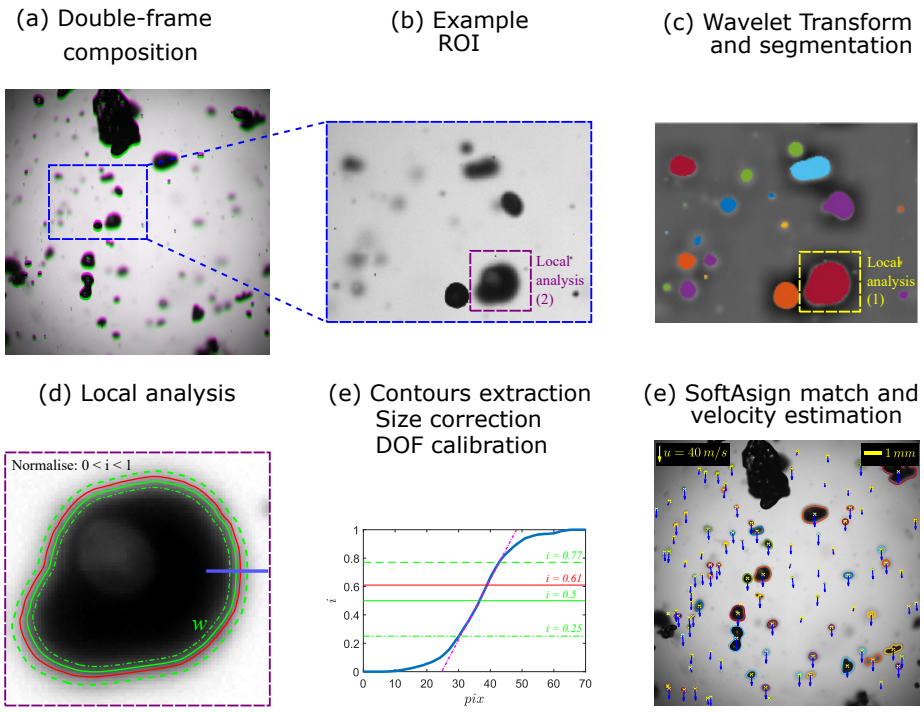

Figure 7: Shadow image segmentation using MATLAB toolboxes. Image post-processing at $[x/d_n = 600,\ y/d_n = 0]$.

The final result of the image segmentation procedure, after wavelet transform and filtering, local analysis, contours extraction and velocity estimation, is shown in Fig. 7-f. The information for every frame is saved for further granulometry and velocimetry analyses of the jet.

4.3.4. Size correction and depth-of-field calibration

Up to here, the custom DTV algorithm is efficient enough to detect very small and large objects in the same image. However, given the general dimensions of the spray, the ability to capture out-of-focus objects has an inconvenient. Indeed, as the defocusing of the objects increases, the error on estimating their true size also increases. Moreover, these out-of-focus droplets in the background or foreground (see Fig. 7-b) may really be far from the detected (x, y) position, as they may be located far from $z = 0$, given the system of coordinates for this

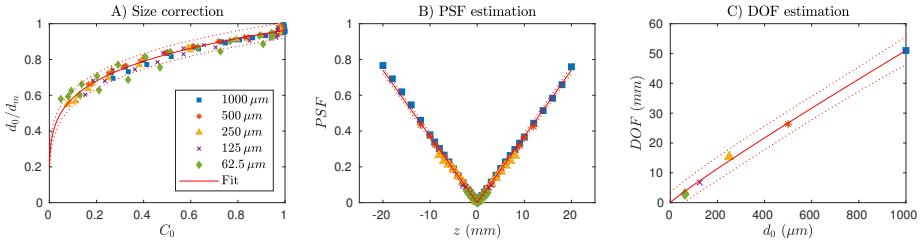

Figure 8: Calibration model for DTV droplets. A) Measured to real size ratio (d_0/d_m) as a function of the normalised contrast ratio (C_0); B) Point-spread-function (PSF) half-width (χ) reconstruction as a function of the focus plane (z); C) Depth-of-field (DOF) estimation as a function of the real size (d_0).

experiment.

As stated in Section 3, the spray presents a cylindrical axisymmetry, meaning that the droplets velocimetry should yield a liquid velocity field in (x, r) coordinates, being r the radial distance to the jet centerline, with $r = \sqrt{y^2 + z^2}$, from the laboratory Cartesian coordinates. It is therefore necessary to identify where, along the z-axis, the aforementioned out-of-focus droplets are, to either correct their real position or eliminate them from the analysis.

Fdida and Blaisot (2010) developed a technique to distinguish those objects, which is based on the idea that, as a function of the defocusing of an object of a given measured size d_m, their position on the z-axis can be estimated by the measured contrast C_0 and the point-spread-function PSF half-width χ, which is a representation of the normalised grey-level gradient at the border of an out-of-focus droplet.

For this, Fig. 8 shows in general the calibration procedure applied to a soda-lime glass grid distortion target (Edmund Optics), where opaque disks painted with nominal diameters d_0 of 62.5, 125, 250, 500 and 1000 μm are measured at several distances from the focus plane (z), emulating the defocusing problem created in this study case. Using the described optical system, Fig. 8-a shows the relation between the measured disk diameter d_m at the grey-level $i = 0.61$, over the known nominal diameter d_0, as a function of the normalised contrast ratio C_0. The choice of $i = 0.61$ is not arbitrary, indeed it was verified that

contrary to the classical threshold $i = 0.50$, the relation obtained by the chosen level yields always an injective relation, meaning that no matter the object nominal size, the ratio $\frac{d_0}{d_m}$ is always less than 1, and monotonically increases with C_0. From this, the following fit is calculated:

$$\frac{d_0}{d_m} = 0.9629 \cdot (C_0)^{0.2166}. \tag{14}$$

Eq. 14 is now referred to as the size correction function. From this, every droplet detected has this function applied to correct its measured size, where the measured size d_m is taken as $d_{[30]}$ from the previous detection algorithm (see Section 4.3.3).

The Depth-of-Field (DOF) estimation is based on the Point-Spread-Function (PSF) half-width χ calculation. The previously measured contours at $w_{i=0.25}$ and $w_{i=0.77}$ allow to estimate the half-width χ at the edge of defocused droplets, assuming that the evolution is linear (see Fig. 7-e). Fig. 8-b gives then a relation for the half-width $\chi\,(mm)$ with the distance to the focus plane z. In the same way as Fdida and Blaisot (2010), this estimation yields a v-shaped relation, no matter the particle size, allowing to clearly establish the position of the object in the z-direction by only measuring χ.

The DOF for an object of size d_0 is given by the Δz_{max} between the v-shaped χ limits, provided that the normalised contrast ratio $C_0 \geq 0.1$. The result is then presented in Fig. 8-c, where the following fitting relation was obtained:

$$DOF = 0.08153 \cdot (d_0)^{0.9321}\ (mm). \tag{15}$$

This relation gives the minimum DOF based on the smallest particle that the imaging DTV system is able to see. In this case, the minimum acceptable object is a round droplet of at least $9\,pix$, equivalent to a $d_{[20]} = 24.5\,\mu m$, which yields a $DOF_{min} = 1.61\,mm$. In this case, $d_{[20]} = \sqrt[2]{\frac{4S_{BW}}{\pi}}$, with S_{BW} the surface of the 9 binary pixels after applying the scale factor. [R01-C12] Comparing this result with a classic sharpness acceptance calculation for the DOF (Salvaggio et al., 2009), using a circle of confusion of 25 μm and a working

distance of 101 mm, the classic approach yields a $DOF_{min} = 0.12\,mm$. This result points out that when considering the out-of-focus calibration presented here, the method allows to detect objects in a significantly larger depth-of-field.

This calibration procedure then provides an extra criterion for analysing every droplet detected in Fig. 7. To eliminate the DOF bias, the PSF half-width is estimated for each object on-the-fly when the detection phase is being conducted; then, a droplet is validated only if it sits inside the thin slice at $DOF_{min} = 1.61\,mm$. In general, this ensures that all of the detected and validated droplets are in the same virtual measurement volume.

4.3.5. Post-processing of DTV data

The information is then treated as independent events on the whole series of 1000 images, where the droplets centroid positions are used to place them in 5 vertical stripes-zones per image, each one of $2.95\,mm\,(y)$. Together with the DOF calibration, the effective measurement volume of the DTV results in $14.73\,mm\,(x) \times 2.95\,mm\,(y) \times 1.61\,mm\,(z)$ increasing the spatial resolution.

[R01-C13] Indeed, if this step was ignored, meaning that out-of-focus droplets are included into the analysis, then two biases would appear. First, because small objects are seen in a much thinner DOF than bigger ones, the population of small droplets would be underestimated. And, secondly, because of the same consequence, by taking into account the cylindrical axisymmetry of the problem, big out-of-focus objects could be detected at a lateral position not matching their real position with respect to the jet centerline.

5. Results

In this section, we will compare the mean and fluctuating velocity fields obtained from both LDV and DTV measurement campaigns to justify the choice of the data used to reconstruct the mixture fields. Then, we will analyse results concerning the flow global properties, such as the way the self-similar regime is attained, in association with the longitudinal evolutions of the decay and spreading rates. Finally, we will also pay specific attention to the mixture

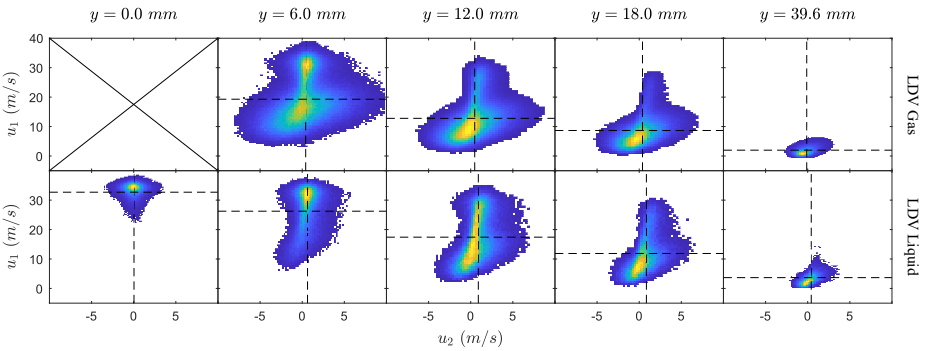

Figure 9: Joint Probability Density Functions (JPDFs) of $u_1 - u_2$ velocities for LDV Gas and LDV Liquid measurement campaigns at $x/d_n = 600$. Black dash lines indicate mean values taken from Eq. A.2-A.4.

quantities and compare them with those for the liquid phase and for the gas phase.

5.1. LDV results

[R03-C15, C19, C28] Raw results from the LDV measurement campaign are shown in Fig. 9, presented as Joint Probability Density Functions (JPDFs) of $u_1 - u_2$ velocities across several radial positions, for both LDV Gas and LDV Liquid measurement campaigns at $x/d_n = 600$. One must recall that no data on the gas phase can be acquired for $y < 6\,mm$ at this streamwise position. The JPDFs show a clear distinction between the water droplets and the gas tracers. Although it was mentioned that a complete separation of small droplets from the olive oil mist cannot be made, the JPDFs show the signature of the liquid pollution inside the gas phase JPDFs, revealing a significant mean slip velocity between the phases. By looking at the magnitude of this slip velocity, it can be concluded that if the gas phase JPDFs could be purged of the pollution from the liquid events, the revealed slip velocity would be even greater in magnitude at any given position for both axial and radial components (see Eq. 11).

The averaged values from the previous JPDFs are then shown explicitly in Fig. 10, [R03-C01] where the notation $\langle u \rangle_1$ for instance is a generic notation which can refer to any type of averaged quantity considered herein (such as Favre

or Reynolds averaged quantity, or averaged quantity related to the gas phase, the liquid phase or the mixture, see Appendix A). As expected, PM intensity and seeding particles have a significant impact on the velocity signal: the blue points (filled squares) corresponding to the liquid with low PM sensitivity are not directly in agreement with the light blue ones (opened squares), corresponding to the liquid with high PM sensitivity. From these results, detecting more very small particles leads to lower longitudinal and radial mean liquid velocities, but higher Reynolds stresses $\bar{R}_{ii}$ (large fluctuations). Along with these results, the previously introduced liquid mass fraction $\widetilde{Y}$ is superimposed to identify the region where the liquid is more present in the radial direction of the spray.

Comparing liquid and gas estimations by component in Fig. 10, the previously mentioned slip-velocity in both longitudinal and radial directions $\bar{u}_{i,S}$ appears along the same radial profile at $x/d_n = 600$ (see Eq. 11). The liquid radial mean velocity is higher than the gas one and it is always positive, showing the liquid spreading outwards. On the contrary, in the outer regions of the jet, the gas radial velocity becomes negative, explicitly showing the ambient air entrainment towards the liquid (jet axis). The liquid and gas have comparable longitudinal Reynolds stresses, but in the radial direction those for the gas are generally higher (about twice those for the liquid).

Even though the gas profiles for $\bar{u}_{i,G}$ and $\bar{R}_{ij,G}$ allow to identify and reconstruct the slip quantities from Eq. 11 and Eq. 10, as previously discussed, these profiles are polluted by water droplets in the averaged quantities, introducing a bias. However, Fig. 10 shows an interesting trend for these results. In general, if there would be no pollution of liquid droplets into gas tracers, the slip-velocity $\bar{u}_{i,S}$ would be expected to be even higher; and $\bar{R}_{22,G}$ would be expected to be even higher and closer to a lower $\bar{R}_{11,G}$.

In order to quantify and understand the effect of the distribution of droplet sizes on these quantities, the detailed experimental campaign using Droplet Tracking Velocimetry (DTV) by shadowgraphy is presented next.

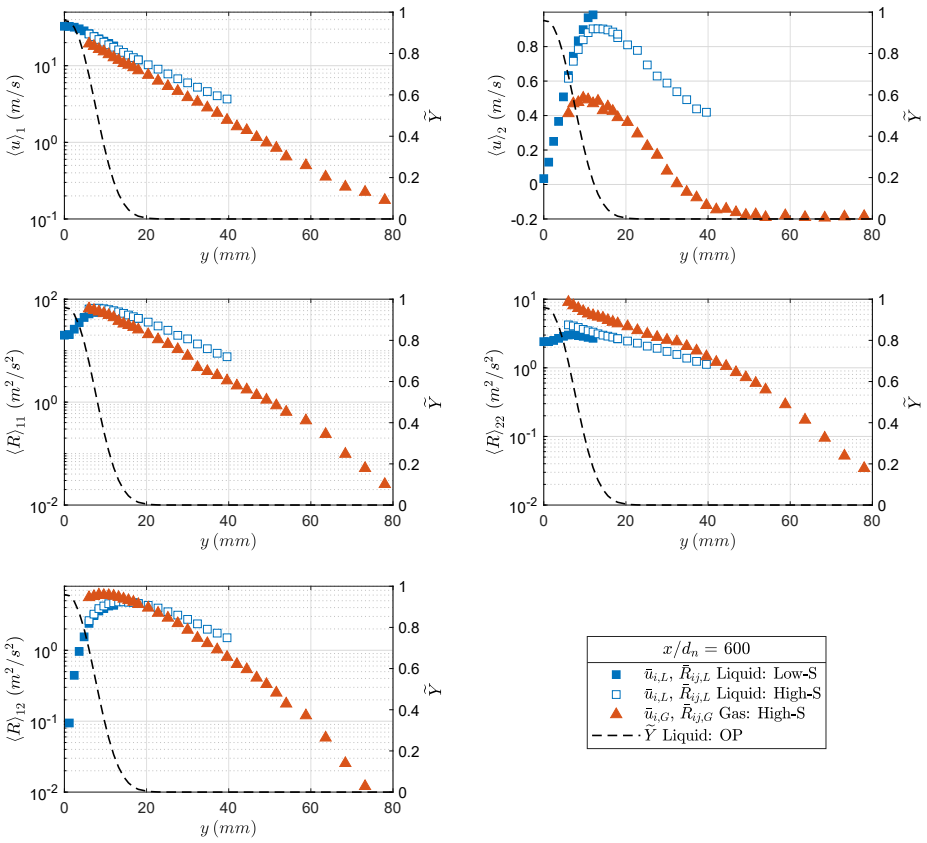

Figure 10: LDV mean velocities and Reynolds stresses profiles at $x/d_n = 600$.

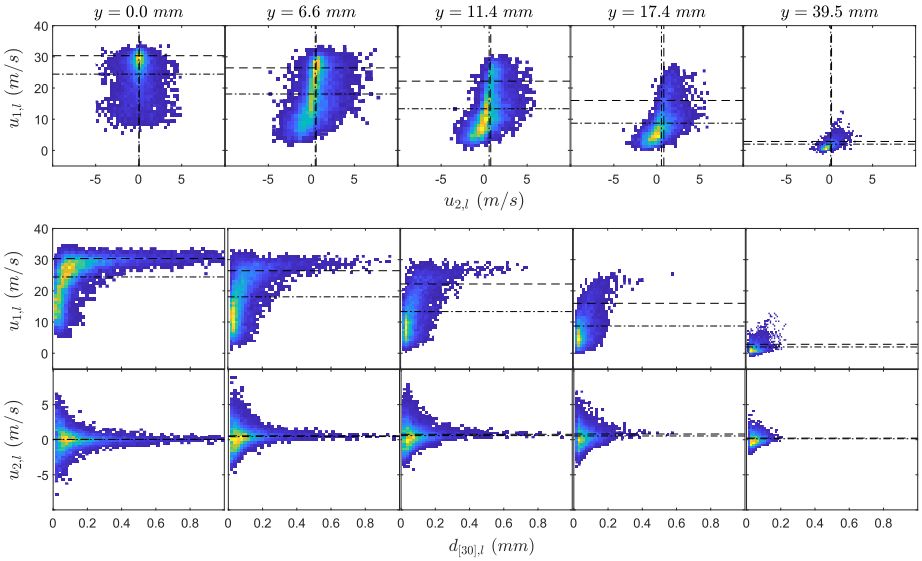

Figure 11: Joint probability density functions (coloured iso-surfaces) obtained from the bi-variate histograms of the components of the droplets velocities $u_{1,l}$ and $u_{2,l}$, and their size $d_{[30],l}$. Data extracted from the DTV analysis in several lateral positions at $x/d_n = 600$. Averaged velocities Eq. A.6 (-. line) and volume-weighted averaged velocities Eq. A.8 (– line).

5.2. DTV results

[R01-C08] [R03-C28] Applying the analysis described in Section 4.3 to the series of images from Fig. 1 (only in the dispersed zone, over the region $x/d_n = 400-600$), the results are the components of the droplets velocities $u_{1,l}$, $u_{2,l}$ and their correctly estimated size $d_{[30],l}$ (where the subscript l refers to any particular droplet, from which averaged quantities are then computed according to the definitions presented in Appendix A). Fig. 11 shows the transverse evolution of the joint probability density functions (JPDFs) for the quantities $u_{1,l} - u_{2,l}$, $u_{1,l} - d_{[30],l}$ and $u_{2,l} - d_{[30],l}$ at $x/d_n = 600$, starting from the centerline of the jet at $y = 0\,mm$, up to $y = 39.5\,mm$ where $\widetilde{Y} \sim 10^{-5}$ (and $\bar{Y} \sim 10^{-8}$, the liquid volume fraction). To graphically illustrate this process, Fig. 6 shows the superposition of images also at $x/d_n = 600$, where a clear evolution of the droplets size and liquid volume fraction can be observed in a way similar to the more quantitative information provided by the JPDFs.

Indeed, Fig. 11 shows that the droplets behaviour strongly depends on their characteristic size. Big droplets (with $d_{[30]} \geq 0.5 - 0.8mm$) are concentrated close to the jet centerline, and are associated with a high mean velocity and limited velocity fluctuations around the mean value; on the contrary, small droplets have a lower mean velocity, but a much larger range of fluctuations, which are also present everywhere across the lateral direction. To better illustrate this effect, Fig. 11 presents two possible approaches for evaluating the mean droplet velocities. The first approach computes the liquid phase mean velocity $\bar{u}_{i,L}$ as the simple arithmetic average of all the droplets velocities (use of Eq. A.6). While the second one, which accounts for the size effect, is constructed as the droplets volume weighted average (using Eq. A.8).

The second approach aims to compensate the bias of the volumetric approach of the measuring technique by shadowgraphy, where, if a perfect instrument of infinitesimal volume of measure was used to determine the liquid phase velocity $\bar{u}_{i,L}$, the probability of the event of finding a packet of liquid should be proportional to d^3 in a 3D space. This bias however has nothing to do with the DOF, because, as established in the calibration procedure, the same thin slice of $1.61\,mm$ is used to account for every focused/defocused measured droplet, making the detection of very small and large objects equally probable.

To analyse in a detailed way the behaviour of droplets by class of diameters, the velocity mean and fluctuation fields properties are shown in Fig. 12 in terms of lateral profiles. Seven classes of sizes were selected to show a complete dynamic range, starting from the biggest droplets for $d_{[30]} > 1\,mm$, down to the smallest ones for $d_{[30]} < 50\,\mu m$. The mean values to construct these profiles are computed using Eq. A.10 for the mean velocity $\bar{u}_{i,(k)}$ of class k and Eq. A.11 for the fluctuations around the mean, to compute the Reynolds stresses $\bar{R}_{ij,(k)}$. Fig. 12 clearly highlights, but in a much more detailed way, the general trends which were discussed in relation to Fig. 11, namely, the fact that the biggest droplets ($d_{[30]} \geq 0.5 - 0.8mm$) are associated with large mean longitudinal velocities and small Reynolds stresses values in comparison with small droplets. Also, the ratio between $\bar{R}_{11,(k)}$ and $\bar{R}_{22,(k)}$ is quite large and equal to about 10

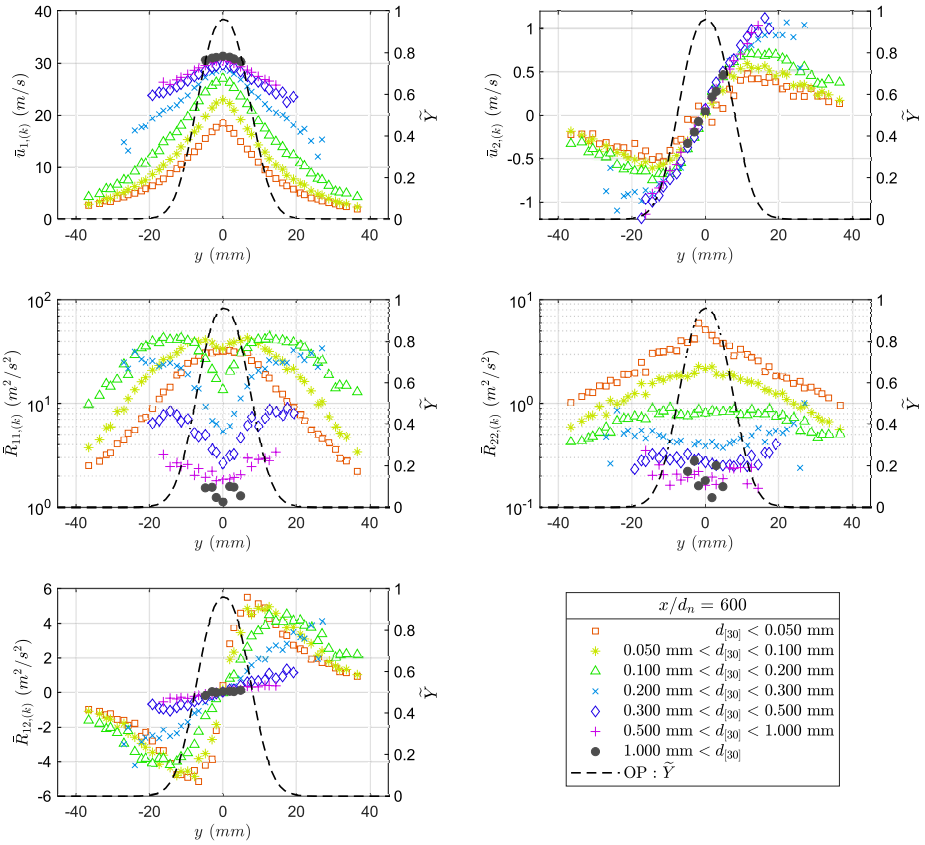

Figure 12: DTV mean velocities by class $\bar{u}_{i,(k)}$ and Reynolds stresses by class $\bar{R}_{ij,(k)}$ at $x/d_n = 600$.

regardless of the droplet size (note that, in relation to this, the vertical ordinates for $\bar{R}_{11,(k)}$ and for $\bar{R}_{22,(k)}$ differ by a factor of 10 to allow direct comparison), with very low values of $\bar{R}_{11,(k)}$ close to the axis for $d_{[30]} > 0.20\,mm$. Only the smallest droplets ($d_{[30]} < 0.05 - 0.10\,mm$) display the familiar almost Gaussian shape for $\bar{R}_{11,(k)}$, with the maximum value reached on the centerline.

As previously established by measurements in the spray using the LDV system, there is a significant mean slip-velocity between the phases ($\bar{u}_{i,S}$). As the attempt to measure in the gas phase was then made via tiny olive-oil tracers ($d_{[30]} \sim 2\,\mu m$), Fig. 12 shows that the behaviour of the smallest class of droplets mimics quite well that for a tracer, for both $\bar{u}_{i,(k)}$ and $\bar{R}_{ij,(k)}$, for

$(k) \in \{d_{[30]} < 50\,\mu m\}$. Because of the liquid droplets polluting the LDV gas data, although this last statement cannot be verified, a special class of droplets for $(k) \in \{d_{[30]} < 30\,\mu m\}$ is used to represent a new gas field tracer. [R03-C29] The droplets of this class are the smallest estimated through DTV, their Stokes number on the centerline is between 3 and 9. Although these droplets should not be considered as gas tracers, they provide the most reliable information about the gas phase (see Felis-Carrasco (2017) for more details). As we are interested in reconstructing the mixture averaged fields (Eq. 7 and Eq. 10), the contribution from the gas phase is smaller close to the jet centerline, where $\widetilde{Y} \sim 1$, resulting in $\tilde{u}_i \sim \bar{u}_{i,L}$ and $\tilde{R}_{ij} \sim \bar{R}_{ij,L}$.

5.3. Mean and fluctuating velocity fields

Fig. 13 underlines that, as previously noticed, big droplets ($d_{[30]} > 1\,mm$) have a behaviour significantly different from that for the smallest ones ($d_{[30]} < 30\,\mu m$). Also of interest is that velocities and Reynolds stresses of these smallest droplets are weaker than those obtained by LDV for the gas phase. This also enforces that LDV on the gas phase is polluted by liquid droplets and justifies to use the DTV data of the smallest droplets to estimate the mixture associated quantities. The distribution of droplets sizes plays a major role in the reconstruction of the mean velocity and Reynolds stress fields. As expected, close to the centerline, the liquid quantities are governed by the big droplets and then tend to the behaviour of the smallest ones for increasing radial distances. LDV and DTV data for the liquid phase are similar, except for $\bar{R}_{22,L}$ where the very low values for big droplets decrease its estimated value [R03-C29] on the centerline.

5.4. Mixture quantities

Fig. 14 reports radial profiles for the mean liquid mass fraction $\tilde{Y}$ and longitudinal and radial mean velocities $\tilde{u}_i$ and Reynolds stresses $\tilde{R}_{ij}$ at $x/d_n = 600$, where the liquid core has disappeared. As expected, the liquid-phase associated quantities are significantly larger than the gas-phase ones, except for $\bar{R}_{22}$ as

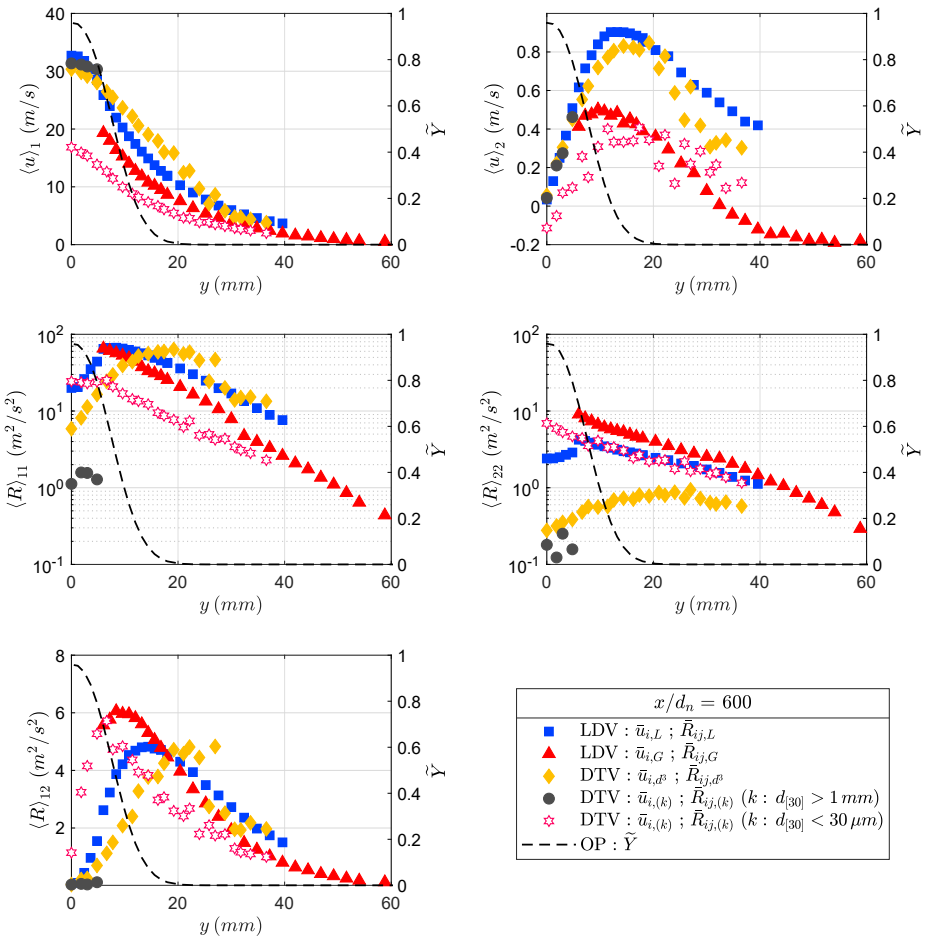

Figure 13: Mean and fluctuating velocity fields at $x/d_n = 600$ obtained by LDV and DTV for the liquid and gas phases.

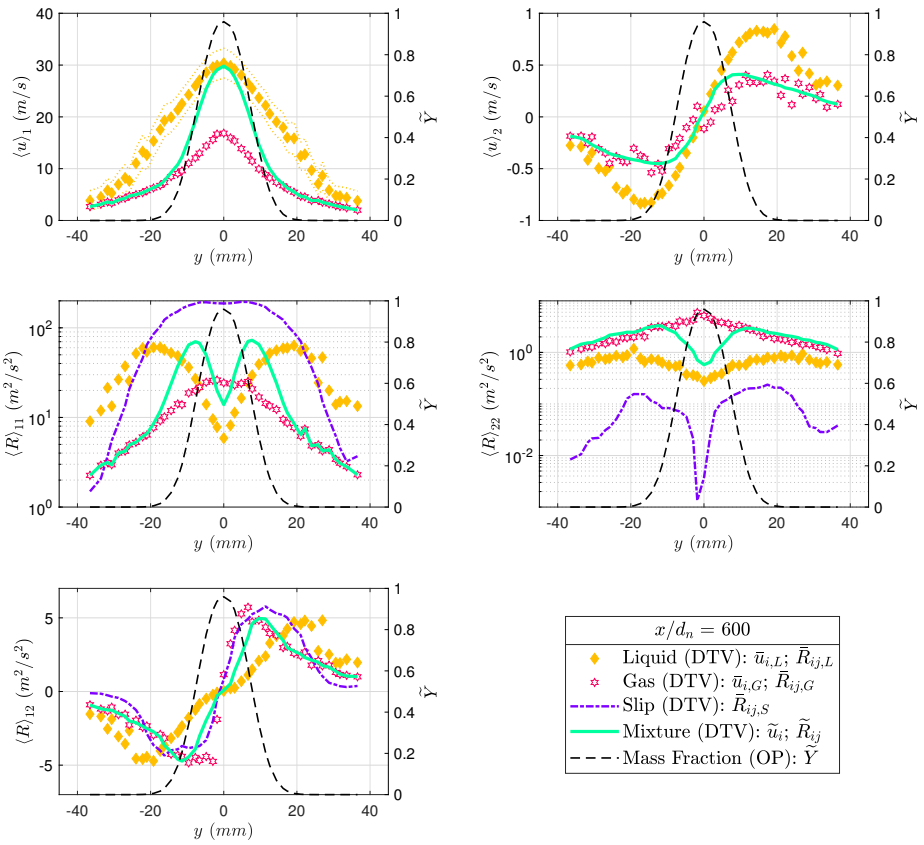

Figure 14: Comparison of results obtained for the jet main properties at $x/d_n = 600$ using the DTV and OP measurements.

already observed due to big droplet inertia. In addition, because of the definition of the Favre-averaged mixture velocity $\tilde{u}_1$, the contribution from the liquid phase to the mixture velocity becomes negligible from the radial position where $\tilde{Y}$ is smaller than about 0.2, while it is largely dominant as long as $\tilde{Y}$ is larger than about 0.6. This underlines that the mixture quantities can not be approximated only by the liquid data (even though they are more convenient to measure). Also, the slip between the two phases is quite important and even strengthens the turbulence anisotropy $\bar{R}_{22}/\bar{R}_{11}$ since its contribution to $\bar{R}_{11}$ is very large.

[R03-C37] The reconstruction of these mixture quantities for this kind of flow

might help to quantify the performance of several numerical models. Indeed, the mixture fluid formulation, using the Favre-averaged mass conservation and momentum equations (Eq. 8 and Eq. 9), is used in many variations of the original formulation derived by Vallet et al. (2001). Since then it has been applied to many industrial flow applications (Demoulin et al., 2007; Lebas et al., 2009; Payri et al., 2015; Andreini et al., 2016), where the turbulent mass fluxes and Reynolds stresses are modelled quantities, requiring sometimes complex closure terms and/or transport equations.

As expressed before, the principal aim of the mixture reconstruction proposed in this work is to provide a baseline database, with which these numerical models can be compared. Just as an example, the turbulence modelling in many of these industrial flow models rely most commonly on a form of $k-\epsilon$ formulation, which assumes that the principal components of the Reynolds stresses are isotropic ($\langle R \rangle_{11} = \langle R \rangle_{22} = \langle R \rangle_{33}$). As previously presented in these results, this is far from the reality for the present case, where $\langle R \rangle_{11} \sim 20 \langle R \rangle_{22}$. The next section aims to provide some basic parameters that would allow to build such comparisons, taking into account the previously reconstructed mean fields.

The uncertainty of the axial component of the liquid velocity field ($\bar{u}_{1,L}$) is also reported in Fig. 14. Using the later fit confidence bounds from Eq. 16 and Eq. 17, along with the discussion on the measurement errors from Section 5.6, it allows to give an estimation for this quantity.

5.5. Flow global properties

For a round-jet, the decay of the centerline velocity and the spreading-rate are some immediate useful parameters to consider, as they set the first baseline to quickly compare the different methods used to characterise the spray. However, it is not straightforward to define a proper velocity field $\langle u \rangle_i$ in the present approach for such parameters. Indeed, as previously shown in Section 2, the mean flow of the spray would be completely characterised if $\bar{u}_{i,L}$, $\bar{u}_{i,G}$ and $\widetilde{Y}$ could be obtained. An approximation using both LDV and DTV measurements with the aim to describe such data was presented in Fig. 13, where a version

of the mean velocity and fluctuating fields for the liquid ($\bar{u}_{i,L}$) and gas ($\bar{u}_{i,G}$) phases is shown along the liquid mass fraction $\widetilde{Y}$. Combining these results, an approximation of the mixture velocity field ($\tilde{u}_i$) was obtained (see Fig. 14).

The decay-rates of the centerline velocities are then calculated using these different approaches. First, the generic velocity field $\langle u \rangle_i$ is associated to the averaged velocity field calculated from the LDV campaign ($\bar{u}_{i,L}$ from Eq. A.2); later, the same is applied but using the DTV ($\bar{u}_{i,d^3}$ from Eq. A.8); and finally the mixture approach using the Favre-averaged reconstructed field ($\tilde{u}_i$ from Eq. 7).

For the velocity field, the decay-rate A is defined as:

$$\frac{\langle u \rangle_{1,0}}{\langle u \rangle_J} = \frac{1}{A} \frac{d_n}{x - x_0} \left(\frac{\rho_L}{\rho_G} \right)^{0.5}, \tag{16}$$

and the spreading-rate S as:

$$\langle y \rangle_{0.5} = S \left(x - x_0 \right). \tag{17}$$

where $\langle y \rangle_{0.5}$ is the velocity (the same holds for the liquid mass fraction) half-width and $\langle u \rangle_{1,0}$ is the value of $\langle u \rangle_1$ at $y = 0mm$.

The spray presently studied is characterised at the same time by a low decay rate of the centerline axial velocity and a low spreading rate (see Fig. 15 and Tab. 3), in comparison with the classical results obtained for single phase jets (Wygnanski and Fiedler, 1969; Ruffin et al., 1994; Hussein et al., 1994). However, the value obtained in our case is quite close to the values measured by Georjon (1998) ($S_{u,L} = 0.025$), Boedec (1999) ($S_{u,L} = 0.021$) and Stevenin et al. (2016) ($S_{u,L} = 0.024$) for sprays.

The difference between the LDV and DTV measurements can be explained by the integration volume over which the data is acquired. For the LDV case, by placing the system in forward scattering mode using a PDA receiving unit, the measurement volume is reduced to $0.15\,mm\,(x) \times 0.15\,mm\,(y) \times 0.20\,mm\,(z)$. On the contrary, for DTV, although the dimensions are reduced by the image sub-frame analysis and DOF calibration, the resulting effective measurement volume is significantly bigger in each direction ($14.73\,mm\,(x) \times 2.95\,mm\,(y) \times 1.61\,mm\,(z)$). For example, since the axial velocity decays against the radial

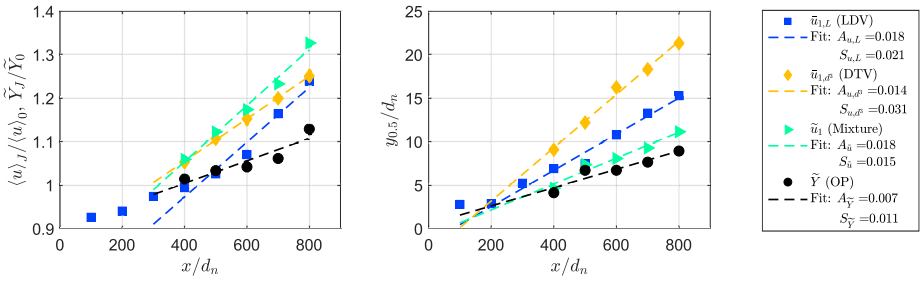

Figure 15: Asymptotic decay-rates and spreading-rates.

	A	S
$\bar{u}_{1,L}$ (LDV)	0.0180	0.0208
$\bar{u}_{1,d^3}$ (DTV)	0.0139	0.0306
$\tilde{u}_1$ (DTV)	0.0184	0.0149
$\widetilde{Y}$ (OP)	0.0074	0.0105

Table 3: Regression coefficients for the decay-rates A and the spreading-rates S.

distance with sharp gradients, this larger integration volume makes the DTV centerline velocity lower than the liquid LDV value.

A self-similar regime is reached rapidly following the rupture of the liquid column, for both phases and thus for the mixture as well (Fig. 16). The radial profiles can be fitted by

$$\frac{\langle u \rangle_1}{\langle u \rangle_{1,0}} = e^{-\beta |\frac{y}{y_{0.5u}}|^\eta} \tag{18}$$

where the β and η values are reported in Tab. 4.

	β	η
$\bar{u}_{1,L}$	0.7086	1.614
$\bar{u}_{1,G}$	0.6619	1.154
$\tilde{u}_1$	0.6437	1.301

Table 4: Coefficients of the self-similar profile fits used in Eq. 18.

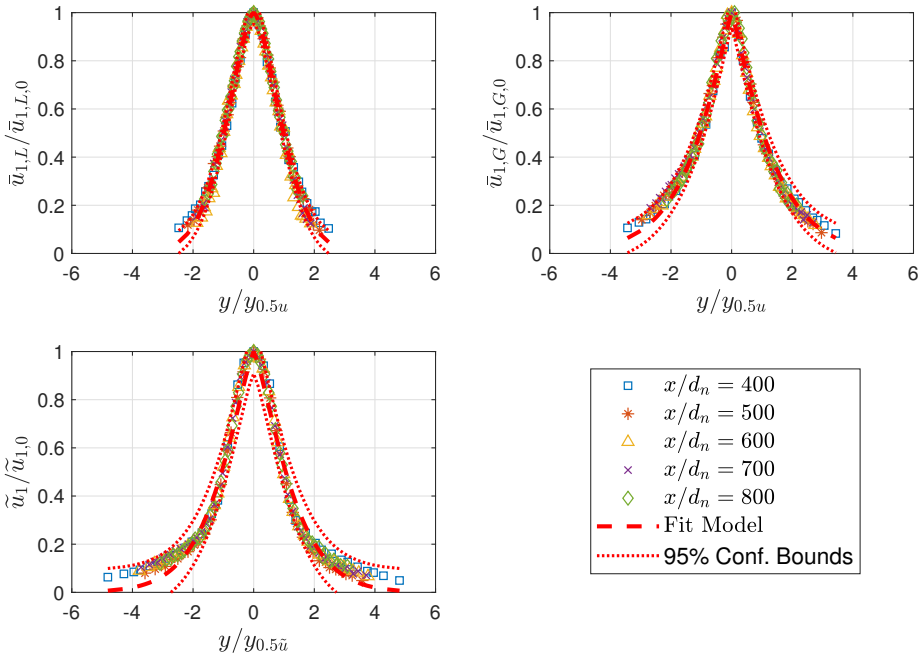

Figure 16: Self-similar profiles of $\langle u \rangle_1$ for the Liquid, Gas and Mixture, issued from the DTV post-process at $x/d_n = 400 - 800$, including the 95% confidence interval from the fit.

Using the self-similar profiles from Fig. 16, together with the decay-rate (A) and spreading-rate (S), the axial component of the velocity field ($\langle u \rangle_1$) for $x/d_n \geq 400$ in polar coordinates (x, r) (from the Cartesian coordinates x_i) can be fully described by:

$$\langle u \rangle_1 (x, r) = \frac{\langle u \rangle_J}{A} \frac{d_n}{(x - x_0)} \left(\frac{\rho_L}{\rho_G} \right)^{0.5} e^{-\beta |\frac{r}{S(x-x_0)}|^\eta} \tag{19}$$

A good likelihood is obtained on both the liquid ($\bar{u}_{1,L}$) and gas ($\bar{u}_{1,G}$) phases for the reconstruction of the velocity fields through Eq. 19. However, because of the apparent non-linear decay and spreading of the liquid mass-fraction ($\widetilde{Y}$) shown in Fig. 15, the mixture velocity field ($\widetilde{u}_1$) presents a slight departure from the fit model proposed using Eq. 18. Moreover, if this representation is accurate, the obtained velocity field should satisfy the continuity equations, Eq. 3 and Eq. 5, for the liquid and gas phases respectively as:

$$\frac{\partial \overline{Y} \bar{u}_{1,L}}{\partial x} + \frac{1}{r} \frac{\partial r \overline{Y} \bar{u}_{r,L}}{\partial r} = 0, \text{ and} \tag{20}$$

$$\frac{\partial \left(1 - \overline{Y}\right) \bar{u}_{1,G}}{\partial x} + \frac{1}{r} \frac{\partial r \left(1 - \overline{Y}\right) \bar{u}_{r,G}}{\partial r} = 0. \tag{21}$$

Nevertheless, even though the liquid volume fraction ($\overline{Y}$) follows a similar form to Eq. 13, these profiles are not found to be self-similar in the range $x/d_n = 400 - 800$, like the velocity counterparts.

This makes it difficult to evaluate algebraically the radial velocities $\bar{u}_{r,L}$ and $\bar{u}_{r,G}$ using the mass conservation from Eq. 20 and Eq. 21 respectively. [R03-C35] [R03-C37] A more refined analysis is required for this particular point which would need the development of a complete self-similarity analysis involving all the different velocities ($\bar{u}_{i,L}$, $\bar{u}_{i,G}$, ...) together with $\overline{Y}$ and $\widetilde{Y}$. This analysis would, hopefully, allow to understand the differences between the A and S values which are displayed in Fig. 15 and Tab. 3. Analysing the role played by the mean slip velocity between the phases, and its connection with the Reynolds stresses, will also be, in that respect, very interesting, through the momentum

conservation equations. But, obviously, such quantitative analyses can not be performed in the present paper.

5.6. Measurement errors

[R02-C02] Having an algebraic form for $\langle u \rangle_1$ allows to estimate the error propagation by taking into account all the variables involved and the instrument uncertainties. Although the systematic and random error could be included into the whole calculation process of mean and fluctuating velocity fields presented here, many assumptions, unknown instrument biases, modelled and fit expressions are introduced across the whole analysis, making the overall error estimation extremely difficult for all the quantities. Therefore, only a global uncertainty was evaluated for the liquid velocity field $\bar{u}_{1,L}$, where a model to represent this was proposed as $\bar{u}_{i,L} \sim \bar{u}_{i,d^3}$.

Starting from the liquid bulk velocity $\bar{u}_J = 35\,m/s$, which was calculated by measuring the liquid flow-rate and then assuming that the nozzle diameter takes the nominal value $d_n = 1.2\,mm$. In reality, although the surface finish of the nozzle was polished with diamond paper to ensure a optical fibre quality, the rounded hole was measured using a calibrated bore gauge, where the actual value was $d_n = 1.21 \pm 0.01\,mm$, transforming into a bulk velocity of $\bar{u}_J = 35 \pm 1.3\,m/s$.

For the OP measurements, the uncertainty of the liquid volume fraction $\overline{Y}$ was estimated to be inferior to 5%. However, the sharp spatial gradients, probe positioning and the fit model introduced to interpolate these results introduce another layer of uncertainties to the liquid mass fraction $\widetilde{Y}$. Although the model seems to accurately describe the experimental points in $\widetilde{Y}$, this expression was evaluated from a phenomenological point of view and not from the underlying physics. Because this experimental campaign was meant to be exploratory, in order to obtain a order of magnitude for the liquid volume fraction $\overline{Y}$ (and mass fraction $\widetilde{Y}$), the values presented here are only given as a reference.

For the LDV system, the Fiber-Flow from Dantec Dynamics reports an uncertainty of 0.067%. However, the velocity statistics results are heavily influenced by the LDV settings, visual access clearance, and flow characteristics. In

this case, the LDV is used to measure a heavy poly-dispersed spray, where the challenges of the experimental setup were previously discussed in Section 4.2. For example, to measure in the liquid phase, the uncertainty associated to the PM high-voltage in the BSA processor can be seen implicitly in Fig. 10 (blue filled squares against open squares). Although not a great difference can be seen in the mean velocity field $\bar{u}_{i,L}$, a significant one is present in the calculated Reynolds stresses $\bar{R}_{ij,L}$.

For the DTV measurements, several assumptions and biases are introduced when introducing the DOF calibration: measured size correction, volume integration, PSF half-width, etc. Although the droplets sizes and velocities are measured initially with great accuracy ($\delta_u \sim 0.13\, m/s$), all droplet sizes are corrected using Eq. 14, introducing a large uncertainty (see fit bounds in Fig. 8-a). As previously shown, from the droplets sizes and velocities statistics, the granulometry of the spray has a big influence on the velocity statistics by class of droplet equivalent diameter (Fig. 12), if biases are introduced in the sizes estimation, then this is propagated towards the spray velocimetry as well.

At the end, a portion of the uncertainty level for the liquid velocity field ($\bar{u}_{i,L} \sim \bar{u}_{i,d^3}$) is shown in Fig. 14, only for the first velocity component. This was constructed assuming that this velocity field is self-similar in the dispersed region of the spray, including the 95% confidence interval from all of the fit parameters (Eq. 16 and Eq. 17). Although only a small portion of the results obtained in the work were shown at $x/d_n = 600$, at the end, Fig. 14 shows a remarkable good collapse of all profiles (for $400 \leq x/d_n \leq 800$), together with a high spatial resolution, clearly revealing more an underlying physics of the spray than the accumulation of random measurement errors. This statement requires however a much deeper analysis at all levels from all the experimental campaigns, with the conclusion that maybe a much more detailed measurement grid, experimental points or more complex calibration models are required to improve the precision and accuracy of the results obtained for the mixture quantities $\tilde{u}_i$ and $\tilde{R}_{ij}$.

6. Conclusion

Three techniques were developed to characterise the atomization and dispersion of an agricultural-like jet in the turbulent atomization regime, for which the liquid core breakup occurs at $x/d_n \approx 200$ and the spray complete formation is achieved by $x/d_n \approx 400$:

- OP to determine the mean volume fraction of the liquid phase;
- a specific LDV configuration to capture the liquid and the gas phases by seeding small olive-oil particles as tracers;
- DTV with a special calibration and a custom algorithm to add more information to the liquid phase related to the distribution of droplet sizes, in the dispersed part of the jet ($x/d_n > 400$).

These experimental methods allow to reconstruct the liquid and gas velocity fields and the mixture quantities in terms of mean velocities and Reynolds stresses. It clearly appears that the droplet size distribution greatly impacts the velocity and the Reynolds stress fields. The spray is characterised by low decay and spreading rates. Self similar profiles of axial velocity are proposed as a function of these decay and spreading rates with a fairly good accordance for the liquid and gas phases and a low divergence for the mixture field data. Turbulence in such a spray is greatly anisotropic for both the liquid and gas phases and thus even more for the mixture. Gas phase dynamics impact the mixture ones, despite the large density ratio ($\rho_L/\rho_G \approx 815$), so that the mixture properties can not be approximated only by the liquid data. The quantities associated with slip between the two phases are also shown to play a significant role in the spray dynamics. Therefore, this work constitutes a precious database for a better understanding of the intricate mechanisms which are involved in the spray formation and for providing further comparison with numerical modelling.

Acknowledgements

This work was funded by the CONICYT PFCHA/DOCTORADO BECAS CHILE/2012 - 72130475, together with the Région Provence-Alpes-Côte dAzur, the European Union (ERDF), IRSTEA (National Research Institute on Science and Technology for Environment and Agriculture - Grant no. DEB 09-1343/2009-22480) and by the Seventh Framework Programme FP7-KBBE-2012-6: Water4Crops. The authors are grateful to the Dantec Dynamics company and especially to Jean-Jacques Lasserre, Hua Wang and Palle Gjelstrup for their collaboration.

Appendix A. Averaged quantities

[R03-C01] The following list summarises all the data averaged quantities used in the present study. Note that the subscript l is used hereafter to represent one particular event (such as a burst for LDV or a droplet for DTV) while n is the total number of events. As used in the text, subscript k refers to a particular class of droplets.

- **Optical Probe**

  Liquid Volume Fraction, where T_a is the total acquisition time and T_l is the time spent over the threshold voltage T_L:

$$\bar{Y} = \frac{1}{T_a} \sum_{l=1}^{n} T_l > T_L. \tag{A.1}$$

- **LDV Liquid**

  Mean velocity:

$$\bar{u}_{i,L} = \frac{1}{n} \sum_{l=1}^{n} u_{i,\{l \in Liq\}}. \tag{A.2}$$

  Velocity Fluctuation:

$$\bar{R}_{ij,L} = \frac{1}{n} \sum_{l=1}^{n} \left(u_{i,\{l \in liq\}} - \bar{u}_{i,L} \right) \left(u_{j,\{l \in liq\}} - \bar{u}_{j,L} \right). \tag{A.3}$$

- **LDV Gas**

  Mean velocity:

$$\bar{u}_{i,G} = \frac{1}{n}\sum_{l=1}^{n} u_{i,\{l\in Gas\}}. \tag{A.4}$$

  Velocity Fluctuation:

$$\bar{R}_{ij,G} = \frac{1}{n}\sum_{l=1}^{n}\left(u_{i,\{l\in gas\}} - \bar{u}_{i,G}\right)\left(u_{j,\{l\in gas\}} - \bar{u}_{j,G}\right). \tag{A.5}$$

- **DTV Liquid**

  Mean velocity:

$$\bar{u}_{i} = \frac{1}{n}\sum_{l=1}^{n} u_{i,l}. \tag{A.6}$$

  Velocity Fluctuation:

$$\bar{R}_{ij} = \frac{1}{n}\sum_{l=1}^{n}\left(u_{i,l} - \bar{u}_{i}\right)\left(u_{j,l} - \bar{u}_{j}\right). \tag{A.7}$$

  Mean Weighted Velocity:

$$\bar{u}_{i,d} = \frac{\sum_{l=1}^{n} d_{[30],l}^{3} u_{i,l}}{\sum_{l=1}^{n} d_{[30],l}^{3}}. \tag{A.8}$$

  Weighted Velocity Fluctuation:

$$\bar{R}_{ij,d} = \frac{\sum_{l=1}^{n} d_{[30],l}^{3}\left(u_{i,l} - \bar{u}_{i}\right)\left(u_{j,l} - \bar{u}_{j}\right)}{\sum_{l=1}^{n} d_{[30],l}^{3}}. \tag{A.9}$$

  Mean Velocity by Class:

$$\bar{u}_{i,(k)} = \frac{1}{n}\sum_{l=1}^{n} u_{i,\{l\in(k)\}}. \tag{A.10}$$

  Velocity Fluctuation by Class:

$$\bar{R}_{ij,(k)} = \frac{1}{n}\sum_{l=1}^{n}\left(u_{i,\{l\in(k)\}} - \bar{u}_{i,(k)}\right)\left(u_{j,\{l\in(k)\}} - \bar{u}_{j,(k)}\right). \tag{A.11}$$

References

Al Heidary M, Douzals J, Sinfort C, Vallet A. Influence of spray characteristics on potential spray drift of field crop sprayers: A literature review. Crop Protection 2014;63:120–30.

Andreini A, Bianchini C, Puggelli S, Demoulin FX. Development of a turbulent liquid flux model for EulerianEulerian multiphase flow simulations. International Journal of Multiphase Flow 2016;81:88–103.

Belhadef A, Vallet A, Amielh M, Anselmet F. Pressure-swirl atomization: Modeling and experimental approaches. International Journal of Multiphase Flow 2012;39:13–20.

Boedec T. Caractérisation d'un spray dense et à grande vitesse par diagnostics optiques. Ph.D. thesis; Ecole Centrale de Lyon; 1999.

Borghi R, Anselmet F. Turbulent multiphase flows with heat and mass transfer. John Wiley & Sons, 2013.

Boutier A. Vélocimétrie laser pour la mécanique des fluides. Lavoisier, 2012.

Buchhave P, George WK, Lumley JL. The measurement of turbulence with the laser-Doppler anemometer. Annual Review of Fluid Mechanics 1979;11:443–503.

Cartellier A. Simultaneous void fraction measurement, bubble velocity, and size estimate using a single optical probe in gas-liquid two-phase flows. Review of Scientific Instruments 1992;63(11):5442–53.

Daves G, Buckius R, Peters J, Schroeder A. Morphology Descriptors of Irregularly Shaped Particles from Two-Dimensional Images. Aerosol Science and Technology 1993;19(2):199–212.

Demoulin FX, Beau PA, Blokkeel G, Mura A, Borghi R. A new model for turbulent flows with large density fluctuations: Application to liquid atomization. Atomization and Sprays 2007;17(4).

Dumouchel C. On the experimental investigation on primary atomization of liquid streams. Experiments in Fluids 2008;45(3):371–422.

Fdida N, Blaisot JB. Drop size distribution measured by imaging: determination of the measurement volume by the calibration of the point spread function. Measurement Science and Technology 2010;21(2):025501.

Felis-Carrasco F. Atomisation et dispersion d'un jet liquide: approches numérique et expérimentale. Ph.D. thesis; Ecole Centrale de Marseille; 2017.

Georjon T. Contribution a l'etude des interactions gouttelettes-gaz dans un ecoulement diphasique de type jet diesel. Ph.D. thesis; Ecole Centrale de Lyon; 1998.

Gold S, Rangarajan A, Lu CP, Pappu S, Mjolsness E. New algorithms for 2D and 3D point matching: pose estimation and correspondence. Pattern Recognition 1998;31(8):1019–31.

Hoyt JW, Taylor JJ. Waves on water jets. Journal of Fluid Mechanics 1977;83(01):119–27.

Hussein HJ, Capp SP, George WK. Velocity measurements in a high-Reynolds-number, momentum-conserving, axisymmetric, turbulent jet. Journal of Fluid Mechanics 1994;258(1994):31–75.

Ishii M. Thermo-fluid dynamics of two-phase flow. DER-EDF, Eyrolles, Paris, 1975.

Joshi JB, Nandakumar K, Evans GM, Pareek VK, Gumulya MM, Sathe MJ, Khanwale MA. Bubble generated turbulence and direct numerical simulations. Chemical Engineering Science 2017;157:26–75.

Lebas R, Menard T, Beau PPA, Berlemont A, Demoulin FFX. Numerical simulation of primary break-up and atomization: DNS and modelling study. International Journal of Multiphase Flow 2009;35(3):247–60.

Mychkovsky AG, Ceccio SL. LDV measurements and analysis of gas and particulate phase velocity profiles in a vertical jet plume in a 2D bubbling fluidized

bed Part II: Mass and momentum transport. Powder Technology 2012;220:47–54.

Mychkovsky AG, Rangarajan D, Ceccio SL. LDV measurements and analysis of gas and particulate phase velocity profiles in a vertical jet plume in a 2D bubbling fluidized bed. Part I: A two-phase LDV measurement technique. Powder Technology 2012;220:55–62.

Otsu N. A threshold selection method from gray-level histograms. IEEE Transactions on Systems, Man, and Cybernetics 1979;9(1):62–6. doi:10.1109/TSMC.1979.4310076.

Özel A, Fede P, Simonin O. Development of filtered eulereuler two-phase model for circulating fluidised bed: High resolution simulation, formulation and a priori analyses. International Journal of Multiphase Flow 2013;55:43–63.

Payri R, Ruiz S, Gimeno J, Martí-Aldaraví P. Verification of a new CFD compressible segregated and multi-phase solver with different flux updates-equations sequences. Applied Mathematical Modelling 2015;39(2):851–61.

Rogers CB, Eaton JK. The behaviour of solid particles in a vertical turbulent boundary layer in air. International Journal of Multiphase Flow 1990;16:819–34.

Ruffin E, Schiestel R, Anselmet F, Amielh M, Fulachier L. Investigation of characteristic scales in variable density turbulent jets using a second-order model. Physics of Fluids 1994;6(8):2785–99.

Salcedo R, Vallet A, Granell R, Garcerá C, Moltó E, Chueca P. Eulerian-Lagrangian model of the behaviour ofdroplets produced by an air-assisted sprayer inacitrus orchard. Biosystems Engineering 2017;154:76–91.

Sallam K, Dai Z, Faeth GG. Liquid breakup at the surface of turbulent round liquid jets in still gases. International Journal of Multiphase Flow 2002;28(3):427–49.

Salvaggio N, Stroebel L, Zakia R. Basic Photographic Materials and Processes. Focal Press/Elsevier, 2009.

Simonin O. Prediction of the dispersed phase turbulence in particle-laden jets. Gas-Solid Flows ASME-FED 1991;121:197–206.

Stevenin C, Tomas S, Vallet A, Amielh M, Anselmet F. Flow characteristics of a large-size pressure-atomized spray using DTV. International Journal of Multiphase Flow 2016;84:264–78.

Vallet A, Burluka AA, Borghi R. Development of a eulerian model for the "atomization" of a liquid jet. Atomization and Sprays 2001;11(6):619–42.

Wu PK, Faeth GM. Onset and end of drop formation along the surface of turbulent liquid jets in still gases. Physics of Fluids 1995;7(11):2915–7.

Wu PK, Tseng LK, Faeth GM. Primary breakup in gas/liquid mixing layers for turbulent liquids. Atomization and Sprays 1992;2(3):295–317.

Wygnanski I, Fiedler H. Some measurements in the self-preserving jet. jfm 1969;38(3):577–612.

Yon J. Jet Diesel Haute Pression en Champ Proche et Lointain : Etude par Imagerie. Ph.D. thesis; Université de Rouen; 2003.